

Dynamics of Wound Closure in Living Nematic Epithelia

Henry Andralojc,^{1,*} Jake Turley,^{1,2,3} Helen Weavers,³ Paul Martin,³ Isaac V. Chenchiah,¹ Rachel R. Bennett,^{1,4,†} and Tanniemola B. Liverpool^{1,4,‡}

¹*School of Mathematics, University of Bristol, Fry Building, Woodland Road, Bristol BS8 1UG, UK*

²*Mechanobiology Institute, National University of Singapore, Singapore, Singapore*

³*School of Biochemistry, University of Bristol, University Walk, Bristol, BS8 1TD, UK*

⁴*Isaac Newton Institute for Mathematical Sciences, 20 Clarkson Rd, Cambridge CB3 0EH, UK*

(Dated: June 11, 2025)

We study theoretically the closure of a wound in a layer of epithelial cells in a living tissue after damage. Our analysis is informed by our recent experiments observing re-epithelialisation *in vivo* of *Drosophila* pupae. On time and length-scales such that the evolution of the epithelial tissue near the wound is well captured by that of a 2D active fluid with local nematic order, we consider the free-surface problem of a hole in a bounded region of tissue, and study the role that active stresses far from the hole play in the closure of the hole. For parallel anchored nematic order at the wound boundary (as we observe in our experiments), we find that closure is accelerated when the active stresses are contractile and slowed down when the stresses are extensile. Parallel anchoring also leads to the appearance of topological defects which annihilate upon wound closure.

Tissue damage triggers a complex series of overlapping cell and tissue movements that are reminiscent of many of the processes found in embryonic morphogenesis [1]. These processes together stave off infection and eventually repair the wound, bringing the tissue back to something approaching its pre-wounded state [2–6]. A key stage of wound healing is re-epithelialisation, in which the epidermal cells at the cut wound edge and the sheet of epithelium behind them advance to seal the wound gap. Individual and concerted cell contractions and *shape changes*, as well as cell *movements* and/or migration and cell *divisions*, all contribute to the closure of the epithelial gap [7–12]. However precisely how much each of these different cell behaviours, and the forces associated with them, contributes to the ultimate wound healing goal is not known. This is because tissue in many organisms are opaque, and hence it is difficult to quantify the contribution of these processes. Therefore the study of translucent tissue from genetically tractable organisms like *Drosophila melanogaster* [9, 13–18], can play a valuable role in leading us towards the required mechanistic understanding of the process [19–21]. The hope is that studying the cellular responses to wounding in such model systems can give insight into mammalian healing, ultimately leading to the development of practices that can aid clinicians and patients [5, 22]. Such studies can also inspire design principles for developing self-healing artificial systems.

Mechanical models for re-epithelialisation typically include active forces based on two actin-based machineries localised at the wound edge [13, 23–27]: (1) the actin ring, a bundle of filaments at the wound edge that constricts, acting as a ‘purse-string’, dragging the surrounding tissue radially inwards [18, 23], and (2) filopodia and lamellipodia, motile extrusions from the leading edge cells that extend into the wound space and drag the cells behind. Both these effects can be modelled by including

additional (active) terms in the boundary conditions at the wound surface [26–29]. Here we present a general theoretical continuum framework for re-epithelialisation that includes the active forces in the bulk (the surrounding tissue) [10, 26, 30–35] – inspired by our recent experiments [11, 36–38].

In these experiments, laser ablation was performed on the *Drosophila* pupa wing epithelium to create an approximately circular wound which was followed using time-lapse confocal microscopy. Cell shapes, motion and divisions were tracked and classified using fluorescent tagging and machine learning [37]. We make a number of key observations (see Figure 1). First, in healthy tissue, the typical cell was found to be elongated, head-tail symmetric and aligned along the long axis of the wing (i.e. with nematic symmetry), with the degree of alignment increasing as the tissue developed [11, 36–38]. Second, the alignment of cells close to the wound edge was aligned tangential to the wound edge rather than the bulk tissue (wing axis) [11, 37]. Third, there was a dramatic decrease in the division rate near a wound [11, 37] following wounding – i.e. the tissue is approximately incompressible shortly after wounding [26]. In the continuum limit, the cell shape can thus be described by a nematic order parameter field and cell motion by an incompressible velocity field. The wounded epithelium can hence be modelled as an incompressible, two-dimensional, active nematic [39–41] with a hole (wound) at its centre with parallel anchoring at the wound edge. On the time-scale of healing in this system (up to ~ 4 hours [11]), the tissue flows like a viscous fluid, but with the possibility of additional active stresses. We explore the effect of the activity of the bulk tissue on wound closure, finding that, for parallel-anchored nematic boundary conditions, contractile active stresses accelerate wound closure while extensile active stresses delay it. Interestingly, we find that parallel anchoring is associated with the appearance of

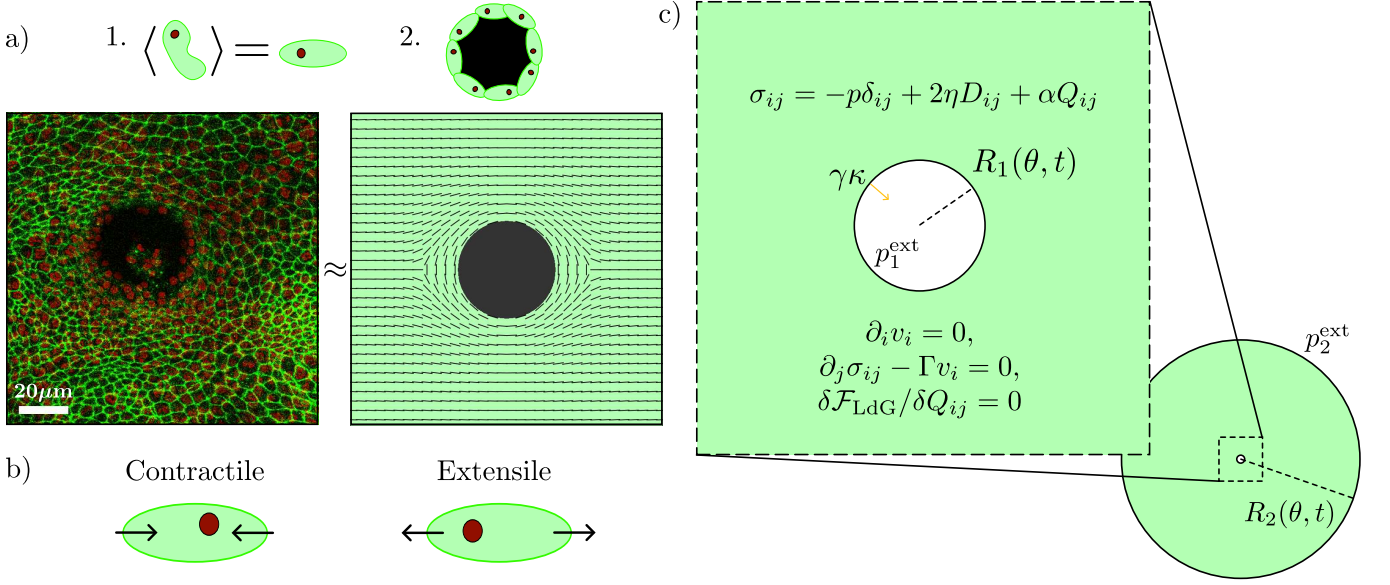


FIG. 1: (a) Schematic illustrating the observations our model is based on. Time-lapse movies of wound healing in *Drosophila* suggest the healthy epithelium has nematic symmetry, aligning along the long axis of the wing. Upon wounding, the cells at the leading edge align parallel to the wound edge. Hence the tissue can be modelled as an active nematic, with parallel anchoring at the wound free boundary. (b) Illustration of active contractile and extensile force dipoles generated on cellular level. (c) Illustration of the model setup.

two $-1/2$ topological defects [42–46] which together with the wound hole, which has topological charge $+1$, annihilate upon closure to leave behind an ‘unscarred’ epithelium with no apparent memory of the wound. We also find that initially circular wounds become anisotropic as the wound closes.

Model. Local cell shape anisotropy is described the traceless symmetric 2×2 tensor field, $\mathbf{Q}(\mathbf{r}, t)$ [47, 48] and motion by an incompressible velocity field, $\mathbf{v}(\mathbf{r}, t)$ and an associated pressure $p(\mathbf{r}, t)$. For isotropic cells, $\mathbf{Q} = 0$ while for elongated cells, $\mathbf{Q} \neq 0$. We study the time-evolution of these fields in a bounded domain following the removal of a circular disc from its center at $t = 0$, using the equations of active nematohydrodynamics at vanishing Reynolds number in contact with a frictional substrate [39, 41, 49, 50]:

$$0 = \nabla \cdot \mathbf{v}, \quad (1a)$$

$$0 = -\nabla p + \eta \nabla^2 \mathbf{v} - \Gamma \mathbf{v} + \alpha \nabla \cdot \mathbf{Q}, \quad (1b)$$

$$0 = \frac{\delta \mathcal{F}_{\text{LdG}}}{\delta \mathbf{Q}}. \quad (1c)$$

where \mathcal{F}_{LdG} is a Landau-de Gennes free energy [41, 47]:

$$\mathcal{F}_{\text{LdG}} = \int d\mathbf{x} \left[-\frac{A}{2} \|\mathbf{Q}\|^2 + \frac{B}{4} \|\mathbf{Q}\|^4 + \frac{K}{2} \|\nabla \mathbf{Q}\|^2 \right], \quad (2)$$

with $\|\mathbf{Q}\|^2 = Q_{ij}Q_{ij}$, $\|\nabla \mathbf{Q}\|^2 = \partial_i Q_{jk} \partial_i Q_{jk}$. η is the bulk viscosity and Γ is the friction coefficient, which we include to model the effect of a basal membrane resisting the flow of the tissue above it. The active stress

$\sigma_{ij}^a = \alpha Q_{ij}$ is present when $\alpha \neq 0$ [41, 51]. We have assumed that \mathbf{Q} relaxes much faster than \mathbf{v} , so the nematic texture is always in a local equilibrium. We consider the wound sufficiently far from the outer wing boundary that it does not affect the wound and choose, for simplicity, an initially circular outer boundary (see Fig. 1). We also ignore elastic contributions to the fluid stress arising due to variations in \mathbf{Q} as they are higher order in gradient and subdominant at long lengthscales [41].

We solve these subject to standard kinematic and dynamic boundary conditions on each free surface, labelled by $r = R_i(\theta, t)$ for $i = 1, 2$ for the inner and outer free surfaces respectively, in addition to conditions on the components of \mathbf{Q} . The dynamic boundary condition (DBC) imposes force balance on every point on the free boundary:

$$[(p_i^{\text{ext}} - p) \mathbf{n} + (2\eta \mathbf{D} + \alpha \mathbf{Q}) \cdot \mathbf{n}]|_{R_i} = \gamma(R_i) \kappa_i \mathbf{n}, \quad (3)$$

where p_i^{ext} is the pressure of the exterior fluid in contact with the i^{th} free surface, $D_{jk} = \frac{1}{2}(\partial_j v_k + \partial_k v_j)$ is the rate of strain tensor [52], \mathbf{n} is the unit normal to the boundary and κ_i is the local curvature of the i^{th} surface. The effective surface tension $\gamma(R_i) = \tilde{\gamma} + \tau(R_i) > 0$ contains both a constant passive surface tension $\tilde{\gamma}$ and an active term $\tau(R_i)$, due to the actin-purse string, which depends on the shape of the wound. We take $\tau(R_i) = \tau$, constant but it is straightforward to treat more complicated scenarios. The kinematic boundary condition (KBC) then governs the time evolution of the free surfaces, requiring

that the flow convects the boundary:

$$D_t[r - R_i(\theta, t)] = 0 \Rightarrow v_r|_{R_i} = \dot{R}_i + \frac{v_\theta|_{R_i}}{R_i} R_i', \quad (4)$$

where $D_t = \partial_t + \mathbf{v} \cdot \nabla$ is the Lagrangian material derivative.

We non-dimensionalise our equations: $\mathbf{r} \rightarrow L\mathbf{r}$, $t \rightarrow Tt$, $p \rightarrow \Pi p$, $\mathbf{Q} \rightarrow Q_0 \mathbf{Q}$ choosing $L = \sqrt{\eta/\Gamma}$, $T = \eta/\Pi$, $\Pi = \gamma/L$, $Q_0 = \sqrt{A/2B}$, and define non-dimensional parameters $\epsilon_\alpha = \alpha Q_0/\Pi$, (relative importance of active to other stresses) and $\Lambda = L/\ell_Q$, (relative sizes of the flow and nematic relaxation length ($\ell_Q^2 = K/2A$) scales). $1/\Lambda$ controls the nematic length scale, and thus the persistence of active forces into the bulk of the fluid.

The wounds in our experiments remain approximately circular throughout re-epithelialisation [38]. Therefore, we solve equations (1) by expanding the dynamical fields in the activity, ϵ_α :

$$R_i(\theta, t) = R_i^0(t) + \epsilon_\alpha R_i^1(\theta, t) \quad (5a)$$

$$\mathbf{v}(r, \theta, t) = \mathbf{v}^0(r, t) + \epsilon_\alpha \mathbf{v}^1(r, \theta, t) + \dots \quad (5b)$$

$$p = p^0 + \epsilon_\alpha p^1 + \dots \quad (5c)$$

$$\mathbf{Q} = \mathbf{Q}^0 + \epsilon_\alpha \mathbf{Q}^1 + \dots, \quad (5d)$$

and decomposing into Fourier modes [53]:

$$R_i^1(\theta, t) = \sum_{n=0}^{\infty} \xi_i^n(t) \cos n\theta + \eta_i^n(t) \sin n\theta, \quad (6)$$

the leading-order problem being a droplet of passive viscous fluid with a circular hole at the centre, whose closure is driven by an (active) surface tension and differences in external pressures. The flow at first order in activity is then additionally driven by leading-order gradients in \mathbf{Q} – i.e. the nematic response to a circular boundary. The magnitude of the active stress in tissue typically cannot be measured directly, and so we cannot confidently claim that ϵ_α is a small parameter, however the fact that the deviations from circular are small in experiment suggest it is *a posteriori*, $\epsilon_\alpha R_i^1/R_i^0 \ll 1$. This continuum approach will of course break down as the wound size approaches the typical cell size and the division rate returns to levels observed in healthy tissue. Therefore, although we solve the equations of motion up to closure, we shall mainly focus on short times following wounding.

Passive bulk tissue with active hole. The flow at leading order is radial by symmetry and independent of \mathbf{Q} . The fluid velocity is then determined by integrating the incompressibility condition (see SI), and using the kinematic boundary condition at the inner boundary to set the constant of integration. Substituting into the Stokes equation at $\mathcal{O}(1)$, the viscous term vanishes, and pressure gradients are balanced by drag, $\nabla p^0 = -\frac{\dot{R}_i^0}{r} \hat{\mathbf{e}}_r$. Integrating the radial component of this equation, we obtain the

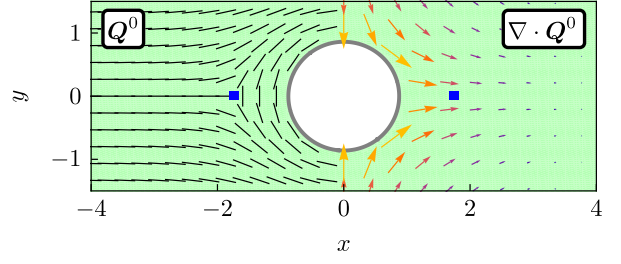


FIG. 2: Nematic texture (left) and active force (right) that appears in the Stokes equation and drives the flow. The size and color of the arrows are used to indicate magnitude. Inset: nematic texture (L) and active driving (R) in the entire domain. The boxed region shows plotted region in main figure and blue squares indicate positions of topological defects. Plotted in a circular geometry, with inner and outer radii of $R_1^0 = 1, R_2^0 = 20$ and ratio of flow : nematic length scales $\Lambda = 0.1$.

pressure. Substituting into the normal component of the DBC at the inner boundary, we obtain an ODE for the inner mode radius which reads, momentarily reinstating dimensional quantities:

$$\dot{R}_1^0 = -\frac{\gamma R_2^0(R_2^0 + R_1^0) + P R_1^0(R_2^0)^2}{2\eta[(R_2^0)^2 - (R_1^0)^2] + \Gamma(R_1^0 R_2^0)^2 \log \frac{R_2^0}{R_1^0}}, \quad (7)$$

where P is the difference in external pressures at the inner and outer boundaries, $P = p_2^{\text{ext}} - p_1^{\text{ext}}$. We see that, at leading order, closure is driven by the effective surface tension (which includes both passive surface tension and active purse-string contributions) and positive pressure differentials ($P > 0$) and is slowed by (dissipative) viscosity and friction or by negative pressure differences ($P < 0$). An illustration the time evolution of $R_1^0(t)$ is given in Fig. 3c.

Nematic Texture and Active Stresses. When we switch on activity ($\alpha \neq 0$), the shape anisotropy, \mathbf{Q} becomes relevant, generating a nematic texture between the inner and outer radii $R_1^0(t), R_2^0(t)$. Minimisation of free energy in eqn. (2) results in a non-linear PDE, which we linearise by expanding around the homogeneous ordered state, aligning with the x -axis: $Q_{xx}^0 = 1 + q_1, Q_{xy}^0 = q_2$, to obtain: $\nabla^2 q_1 - \Lambda^2 q_1 \approx 0$, $\nabla^2 q_2 \approx 0$, a good approximation provided $|q_1|, |q_2| \ll 1$. We take parallel anchoring conditions on R_1^0 , $q_1|_{R_1^0} = -1 - \beta_1 \cos 2\theta$, $q_2|_{R_1^0} = -\beta_1 \sin 2\theta$, and x -axis alignment conditions on R_2^0 , $q_1|_{R_2^0} = -1 + \beta_2$, $q_2|_{R_2^0} = 0$, where $\beta_i = S_i/(2Q_0)$ is the rescaled scalar order parameter at the i^{th} free surface. We obtain an active stress distribution given by

$$\begin{aligned} \nabla \cdot \mathbf{Q}^0 = & -[G_2(r) \sin(2\theta) + G_4(r) \sin(4\theta)] \hat{\mathbf{e}}_\theta \\ & + [G_0(r) + G_2(r) \cos(2\theta) + G_4(r) \cos(4\theta)] \hat{\mathbf{e}}_r. \end{aligned} \quad (8)$$

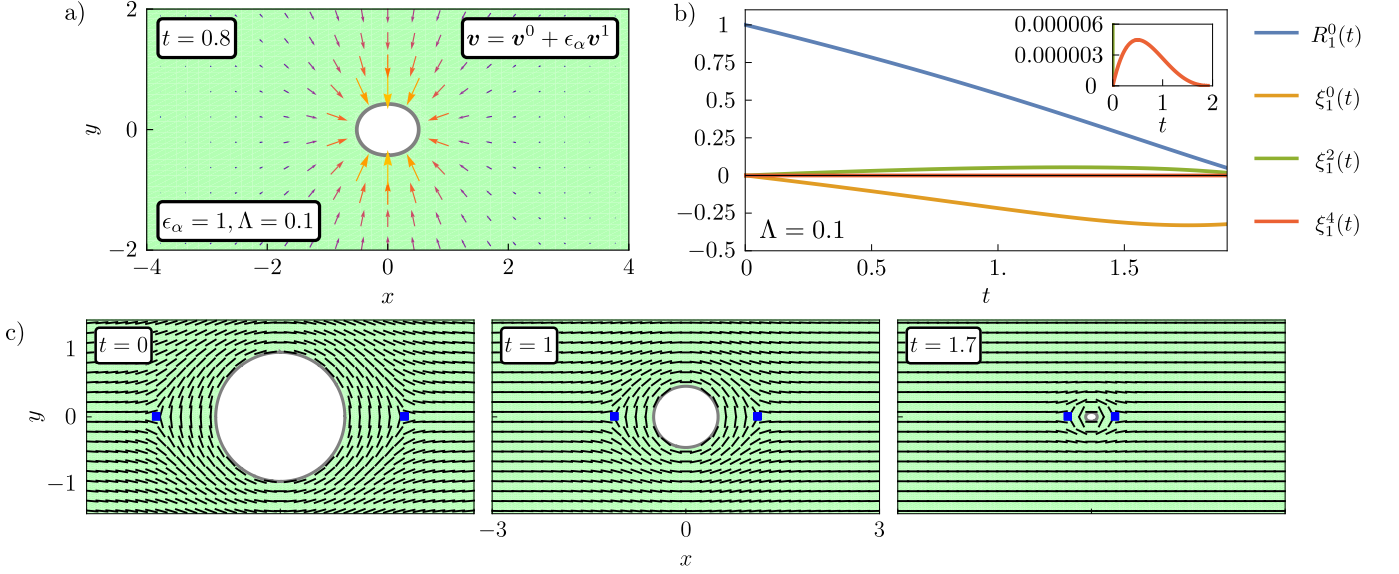


FIG. 3: a) Snapshot of the flow and inner boundary shape, plotted using $\epsilon_\alpha = 1$ to emphasise non-circularity and anisotropy in the flow. (b) Time evolution of inner (wound) boundary shape mode amplitudes throughout closure. The inner boundary is parameterised by $r = R_1(\theta, t) = R_1^0(t) + \epsilon_\alpha (\xi_1^0(t) + \xi_1^2(t) \cos 2\theta + \xi_1^4(t) \cos 4\theta)$. Since $\xi_1^0 \leq 0$ throughout, $\epsilon_\alpha > 0$ accelerates closure of the inner boundary, $\epsilon_\alpha < 0$ hinders closure. (c) Snapshots of nematic texture surrounding the wound boundary during closure ($\Lambda = 0.1$). Blue squares mark the locations of the two $-\frac{1}{2}$ topological defects, which move inwards, following the inner boundary as the hole closes, annihilating and leaving a topologically ‘healed’ state following closure

See SI for the expressions for $G_i(r, \Lambda)$. We point out the presence of $n = 0, 2$ and 4 modes in the driving force appearing in the Stokes equation at $\mathcal{O}(\epsilon_\alpha)$. Figure 2 shows an example of the nematic texture, and active driving $\nabla \cdot \mathbf{Q}^0$ in a fluid domain with $R_1^0 = 1, R_2^0 = 20$ and $\Lambda = 0.1$. We also highlight the presence of two $-\frac{1}{2}$ topological defects in the alignment field surrounding the inner boundary. As the wound closes, the $-\frac{1}{2}$ defects move towards its centre. Since the wound itself provides an additional $+1$ topological charge, upon wound closure, the tissue is in a topologically neutral ‘healed’ state. An illustration of the defect motion during closure is illustrated in Figure 3c.

Activity drives closure and non-circular wound shapes. To compactly express the flow at $\mathcal{O}(\epsilon_\alpha)$, it is convenient to use the stream function $\mathbf{v}^1 = \nabla \times (\psi^1 \hat{\mathbf{e}}_z)$ of the velocity field. Taking the curl of the Stokes equation at $\mathcal{O}(\epsilon_\alpha)$, the stream function satisfies a driven, modified biharmonic equation:

$$\nabla^4 \psi^1 - \nabla^2 \psi^1 = F_2(r, \Lambda) \sin 2\theta + F_4(r, \Lambda) \sin 4\theta. \quad (9)$$

See SI for the expressions for $F_i(r, \Lambda)$. Having obtained the general solution to equation (9), we substitute the velocity into the Stokes equation and integrate for the pressure. The unknown constants in the expressions for the stream function and pressure are then set by the DBCs, equations (3), at each boundary. Having determined the velocity field, we substitute into the KBC at

each boundary to obtain a series of ODEs for the dynamics of shape mode amplitudes, $\dot{\xi}_i^n, \dot{\eta}_i^n, n = 0, 2, 4$ (see eqn. 6, eqn. S36). See SI for explicit equations, calculational details and links to code.

Crucially, we observe that all shape mode amplitudes have a relaxation component to their dynamics, arising from the tendency of surface tension to smooth deviations from circular, but we also have non-trivial driving in the circular ($n = 0$) and quadrupolar ($n = 2, 4$) modes, arising from the active forces in the bulk. These ODEs can be integrated numerically to determine the shape and thus the fluid velocity in the bulk. Figure 3b shows the numerical solution to mode amplitude equations for circular initial conditions $R_1^0 = 1, R_2^0 = 20, \xi_i^n = \eta_i^n = 0 \forall n$, together with a snapshot of the wound boundary shape and surrounding flow in Fig. 3a. A relatively large value of ϵ_α has been used for visualization to emphasize the anisotropy in the flow and shape of the wound boundary.

Discussion: Since the area enclosed by the inner boundary (i.e. the wound size) $A_{\text{wound}}(t)/\pi = (R_1^0)^2 + 2\epsilon_\alpha R_1^0 \xi_1^0 + \mathcal{O}(\epsilon_\alpha^2)$ and $\xi_1^0 \leq 0$ throughout closure (see Fig. 3b), we conclude that positive values of $\epsilon_\alpha > 0$ (corresponding to contractile active stresses) *accelerate closure*, whereas $\epsilon_\alpha < 0$ (extensile) will act to *delay closure*. This is a result of the parallel anchoring condition on \mathbf{Q} at the wound free surface (see Fig. S4). With this anchoring condition, the wound healing process is also associated with the motion of two $-1/2$ topological de-

fects. This is the first of our main results.

Our second main result is that stresses of the form $\nabla \cdot \mathbf{Q}^0$ drive the free surfaces away from circular, as highlighted by non-trivial dynamics of shape mode amplitudes $\xi_1^{2,4}(t)$ in Figure 3b. This is an interesting conclusion, as it suggests that biochemical perturbations which affect anisotropy of the wounds can be used to parametrise the microscopic chemo-mechanics of the wound healing process [37]. Even without a systematic perturbation analysis, the observation that our experimental wounds remain approximately circular supports another conclusion from our model. That is, the inner free boundary remains closer to circular in a fluid with a longer nematic length scale (smaller Λ) – see Fig. S3. Therefore, to reproduce the almost circular wounds observed in our experiments, the effective nematic length scale of the tissue must be relatively large, in agreement with our observations of nematic alignment correlations in the tissue [38].

Conclusion: Informed by experimental observations of re-epithelialisation, we have solved the free-boundary problem of a closing hole in an active nematic fluid. We find that an interplay between boundary conditions on the nematic texture at the wound and the contractile or extensile active stresses in the bulk tissue can significantly affect the speed of healing. It is interesting to speculate whether organisms such as *Drosophila* could use this mechanism to improve the efficacy of the wound healing process.

TBL, JT, IVC, RRB, HA would like to thank the Isaac Newton Institute for Mathematical Sciences, Cambridge, for support and hospitality during the programme *New statistical physics in living matter*, where part of this work was done. This work was supported by EPSRC grants EP/R014604/1 and EP/T031077/1. HA acknowledges the support of an EPSRC studentship and thanks Luke Neville for helpful discussions and advice regarding calculational details. JT is supported by the Eric and Wendy Schmidt AI in Science Postdoctoral Fellowship. This work was carried out using the computational facilities of the Advanced Computing Research Centre, University of Bristol.

* h.andralojc@bristol.ac.uk

† rachel.bennett@bristol.ac.uk

‡ t.liverpool@bristol.ac.uk

- [1] C. Collinet and T. Lecuit, Programmed and self-organized flow of information during morphogenesis, *Nature Reviews Molecular Cell Biology* **22**, 245 (2021).
- [2] G. C. Gurtner, S. Werner, Y. Barrandon, and M. T. Longaker, Wound repair and regeneration, *Nature* **453**, 314 (2008).
- [3] S. A. Eming, P. Martin, and M. Tomic-Canic, Wound repair and regeneration: Mechanisms, signaling, and trans-
- lation, *Science Translational Medicine* **6**, 265sr6 (2014).
- [4] O. A. Peña and P. Martin, Cellular and molecular mechanisms of skin wound healing, *Nature Reviews Molecular Cell Biology* **25**, 599 (2024).
- [5] K. E. Degen and R. G. Gourdie, Embryonic wound healing: A primer for engineering novel therapies for tissue repair, *Birth Defects Research Part C: Embryo Today: Reviews* **96**, 258 (2012).
- [6] P. Martin and R. Nunan, Cellular and molecular mechanisms of repair in acute and chronic wound healing, *British Journal of Dermatology* **173**, 370 (2015).
- [7] S. Park, D. G. Gonzalez, B. Guirao, J. D. Boucher, K. Cockburn, E. D. Marsh, K. R. Mesa, S. Brown, P. Rombolas, A. M. Haberman, Y. Bellaïche, and V. Greco, Tissue-scale coordination of cellular behaviour promotes epidermal wound repair in live mice, *Nature Cell Biology* **19**, 155 (2017).
- [8] M. Aragona, S. Dekoninck, S. Rulands, S. Lenglez, G. Mascré, B. D. Simons, and C. Blanpain, Defining stem cell dynamics and migration during wound healing in mouse skin epidermis, *Nature Communications* **8**, 14684 (2017).
- [9] W. Razzell, W. Wood, and P. Martin, Recapitulation of morphogenetic cell shape changes enables wound re-epithelialisation, *Development* **141**, 1814 (2014).
- [10] R. J. Tetley, M. F. Staddon, D. Heller, A. Hoppe, S. Banerjee, and Y. Mao, Tissue fluidity promotes epithelial wound healing, *Nature Physics* **15**, 1195 (2019).
- [11] J. Turley, F. Robertson, I. V. Chenchiah, T. B. Liverpool, H. Weavers, and P. Martin, Deep learning reveals a damage signalling hierarchy that coordinates different cell behaviours driving wound re-epithelialisation, *Development* **151**, dev202943 (2024).
- [12] B. Garcia-Fernandez, I. Campos, J. Geiger, A. C. Santos, and A. Jacinto, Epithelial resealing, *The International Journal of Developmental Biology* **53**, 1549 (2009).
- [13] W. Wood, A. Jacinto, R. Grose, S. Woolner, J. Gale, C. Wilson, and P. Martin, Wound healing recapitulates morphogenesis in *Drosophila* embryos, *Nature Cell Biology* **4**, 907 (2002).
- [14] M. J. Galko and M. A. Krasnow, Cellular and Genetic Analysis of Wound Healing in *Drosophila* Larvae, *PLOS Biology* **2**, 10.1371/journal.pbio.0020239 (2004).
- [15] H. Weavers, J. Liepe, A. Sim, W. Wood, P. Martin, and M. P. H. Stumpf, Systems Analysis of the Dynamic Inflammatory Response to Tissue Damage Reveals Spatiotemporal Properties of the Wound Attractant Gradient, *Current Biology* **26**, 1975 (2016).
- [16] M. Rämets, R. Lanot, D. Zachary, and P. Manfrulli, JNK Signaling Pathway Is Required for Efficient Wound Healing in *Drosophila*, *Developmental Biology* **241**, 145 (2002).
- [17] A. Franz, W. Wood, and P. Martin, Fat Body Cells Are Motile and Actively Migrate to Wounds to Drive Repair and Prevent Infection, *Developmental Cell* **44**, 460 (2018).
- [18] J. McCluskey, J. Hopkinson-Woolley, B. Luke, and P. Martin, A study of wound healing in the E11.5 mouse embryo by light and electron microscopy, *Tissue and Cell* **25**, 173 (1993).
- [19] W. Razzell, W. Wood, and P. Martin, Swatting flies: modelling wound healing and inflammation in *Drosophila*, *Disease Models & Mechanisms* **4**, 569 (2011).
- [20] V. Muñoz-Soriano, S. López-Domenech, and N. Paricio, Why mammalian wound-healing researchers may wish to turn to *Drosophila* as a model, *Experimental Dermatology*

- 23**, 538 (2014).
- [21] J. Turley, I. V. Chenchiah, T. B. Liverpool, H. Weavers, and P. Martin, What good is maths in studies of wound healing?, *iScience* **25**, 104778 (2022).
 - [22] K. J. Sonnemann and W. M. Bement, Wound Repair: Toward Understanding and Integration of Single-Cell and Multicellular Wound Responses, *Annual Review of Cell and Developmental Biology* **27**, 237 (2011).
 - [23] P. Martin and J. Lewis, Actin cables and epidermal movement in embryonic wound healing, *Nature* **360**, 179 (1992).
 - [24] M. Tamada, T. D. Perez, W. J. Nelson, and M. P. Sheetz, Two distinct modes of myosin assembly and dynamics during epithelial wound closure, *Journal of Cell Biology* **176**, 27 (2007).
 - [25] M. Poujade, E. Grasland-Mongrain, A. Hertzog, J. Jouanneau, P. Chavrier, B. Ladoux, A. Buguin, and P. Silberzan, Collective migration of an epithelial monolayer in response to a model wound, *Proceedings of the National Academy of Sciences* **104**, 15988 (2007).
 - [26] O. Cochet-Escartin, J. Ranft, P. Silberzan, and P. Marcq, Border Forces and Friction Control Epithelial Closure Dynamics, *Biophysical Journal* **106**, 65 (2014).
 - [27] L. Almeida, P. Bagnierini, and A. Habbal, Modeling actin cable contraction, *Computers & Mathematics with Applications Mathematical Methods and Models in Biosciences*, **64**, 310 (2012).
 - [28] J. C. Arciero, Q. Mi, M. F. Branca, D. J. Hackam, and D. Swigon, Continuum Model of Collective Cell Migration in Wound Healing and Colony Expansion, *Biophysical Journal* **100**, 535 (2011).
 - [29] S. Mark, R. Shlomovitz, N. S. Gov, M. Poujade, E. Grasland-Mongrain, and P. Silberzan, Physical Model of the Dynamic Instability in an Expanding Cell Culture, *Biophysical Journal* **98**, 361 (2010).
 - [30] P. Lee and C. W. Wolgemuth, Crawling Cells Can Close Wounds without Purse Strings or Signaling, *PLOS Computational Biology* **7**, e1002007 (2011).
 - [31] C. Villeneuve, K. P. McCreery, and S. A. Wickström, Measuring and manipulating mechanical forces during development, *Nature Cell Biology* **27**, 575 (2025).
 - [32] B. Ladoux and R.-M. Mège, Mechanobiology of collective cell behaviours, *Nature Reviews Molecular Cell Biology* **18**, 743 (2017).
 - [33] R. Etournay, M. Popović, M. Merkel, A. Nandi, C. Blasse, B. Aigouy, H. Brandl, G. Myers, G. Salbreux, F. Jülicher, and S. Eaton, Interplay of cell dynamics and epithelial tension during morphogenesis of the *Drosophila* pupal wing, *eLife* **4**, e07090 (2015).
 - [34] J. Comelles, S. S. S., L. Lu, E. Le Maout, S. Anvitha, G. Salbreux, F. Jülicher, M. M. Inamdar, and D. Riveline, Epithelial colonies in vitro elongate through collective effects, *eLife* **10**, e57730 (2021).
 - [35] E.-M. Schötz, M. Lanio, J. A. Talbot, and M. L. Manning, Glassy dynamics in three-dimensional embryonic tissues, *Journal of The Royal Society Interface* **10**, 20130726 (2013).
 - [36] M. Olenik, J. Turley, S. Cross, H. Weavers, P. Martin, I. V. Chenchiah, and T. B. Liverpool, Fluctuations of cell geometry and their nonequilibrium thermodynamics in living epithelial tissue, *Physical Review E* **107**, 014403 (2023).
 - [37] J. Turley, I. V. Chenchiah, P. Martin, T. B. Liverpool, and H. Weavers, Deep learning for rapid analysis of cell divisions in vivo during epithelial morphogenesis and repair, *eLife* **12**, RP87949 (2024).
 - [38] J. Turley, *Deep learning and mathematical analysis of wound healing in flies; Live imaging in Drosophila*, Ph.D. thesis, University of Bristol (2023).
 - [39] A. Doostmohammadi, J. Ignés-Mullol, J. M. Yeomans, and F. Sagués, Active nematics, *Nature Communications* **9**, 3246 (2018).
 - [40] S. Ramaswamy, The Mechanics and Statistics of Active Matter, *Annual Review of Condensed Matter Physics* **1**, 323 (2010).
 - [41] M. C. Marchetti, J. F. Joanny, S. Ramaswamy, T. B. Liverpool, J. Prost, M. Rao, and R. A. Simha, Hydrodynamics of soft active matter, *Reviews of Modern Physics* **85**, 1143 (2013).
 - [42] D. Dell’Arciprete, M. L. Blow, A. T. Brown, F. D. C. Farrell, J. S. Lintuvuori, A. F. McVey, D. Marenduzzo, and W. C. K. Poon, A growing bacterial colony in two dimensions as an active nematic, *Nature Communications* **9**, 4190 (2018).
 - [43] L. A. Hoffmann, L. N. Carenza, J. Eckert, and L. Giomi, Theory of defect-mediated morphogenesis, *Science Advances* **8**, eabk2712 (2022).
 - [44] K. Kawaguchi, R. Kageyama, and M. Sano, Topological defects control collective dynamics in neural progenitor cell cultures, *Nature* **545**, 327 (2017).
 - [45] Y. Maroudas-Sacks, L. Garion, L. Shani-Zerbib, A. Livshits, E. Braun, and K. Keren, Topological defects in the nematic order of actin fibres as organization centres of Hydra morphogenesis, *Nature Physics* **17**, 251 (2021).
 - [46] T. B. Saw, A. Doostmohammadi, V. Nier, L. Kocgozlu, S. Thampi, Y. Toyama, P. Marcq, C. T. Lim, J. M. Yeomans, and B. Ladoux, Topological defects in epithelia govern cell death and extrusion, *Nature* **544**, 212 (2017).
 - [47] P. G. de Gennes, Short Range Order Effects in the Isotropic Phase of Nematics and Cholesterics, *Molecular Crystals and Liquid Crystals* **12**, 193 (1971).
 - [48] P. M. Chaikin and T. C. Lubensky, *Principles of Condensed Matter Physics* (Cambridge University Press, Cambridge, 1995).
 - [49] A. N. Beris and B. J. Edwards, *Thermodynamics of Flowing Systems: with Internal Microstructure* (Oxford University Press, 1994).
 - [50] M. E. Cates and E. Tjhung, Theories of binary fluid mixtures: from phase-separation kinetics to active emulsions, *Journal of Fluid Mechanics* **836**, P1 (2018).
 - [51] R. A. Simha and S. Ramaswamy, Hydrodynamic Fluctuations and Instabilities in Ordered Suspensions of Self-Propelled Particles, *Physical Review Letters* **89**, 058101 (2002).
 - [52] G. K. Batchelor, *An Introduction to Fluid Dynamics*, Cambridge Mathematical Library (Cambridge University Press, 2000).
 - [53] R. Alert, Fingering instability of active nematic droplets, *Journal of Physics A: Mathematical and Theoretical* **55**, 234009 (2022).

Dynamics of Wound Closure in Living Nematic Epithelia Supplementary Information

Henry Andralojc,^{1,*} Jake Turley,^{1,2,3} Helen Weavers,³ Paul Martin,³ Isaac V. Chenchiah,¹ Rachel R. Bennett,^{1,4,†}
and Tanniemola B. Liverpool^{1,4,‡}

¹*School of Mathematics, University of Bristol, Bristol, BS8 1UG, United Kingdom*

²*Mechanobiology Institute, National University of Singapore, Singapore, Singapore*

³*School of Biochemistry, University of Bristol, University Walk, Bristol, BS8 1TD, UK*

⁴*Isaac Newton Institute for Mathematical Sciences, 20 Clarkson Rd, Cambridge CB3 0EH, UK*

MODEL SETUP

Inner and Outer Boundary

As discussed in the main text, we model the epithelium as an incompressible active nematic fluid. The assumption of incompressibility is the result of our observation of a decrease in the cellular division rate in wounded tissue immediately after wounding [S1]. In order to have a well-posed mathematical problem, we specify the boundary conditions in all our fields at the wound ‘inner’ boundary ($r = R_1(\theta, t)$) but note also that due to incompressibility, we also need to specify the conditions at the outer boundary ($r = R_2(\theta, t)$) of the tissue. We therefore track the evolution of both free-surfaces, and the balance fluxes due to incompressibility at the inner/outer boundaries (for axisymmetric situations) implies that $R_1 v_r|_{R_1} \stackrel{\text{KBC}}{=} R_2 v_r|_{R_2}$ so provided $R_2 \gg R_1 \Rightarrow \dot{R}_2 \ll \dot{R}_1$. As we note below, for realistic situations, the results do not depend appreciably on the conditions at outer boundary.

Equations of Motion and Boundary Conditions

We model the flow of tissue surrounding the wound using the equations of active nematohydrodynamics at vanishing Reynolds number:

$$0 = \nabla \cdot \mathbf{v} , \quad (\text{S1a})$$

$$0 = -\Gamma \mathbf{v} + \nabla \cdot \boldsymbol{\sigma} , \quad (\text{S1b})$$

$$0 = \frac{\delta \mathcal{F}_{\text{LdG}}}{\delta \mathbf{Q}} . \quad (\text{S1c})$$

taking

$$\sigma_{ij} = -p\delta_{ij} + \eta(\partial_i v_j + \partial_j v_i) + \alpha Q_{ij} , \quad (\text{S2})$$

where \mathbf{v}, p are the fluid velocity and pressure respectively and \mathbf{Q} is the tensorial nematic order parameter describing local alignment of cells in the tissue. η is the bulk viscosity and Γ is the frictional coefficient, included to model the resistance to flow due to the presence of a substratum below the epithelium. We take Landau-de Gennes free energy:

$$\mathcal{F}_{\text{LdG}} = \int d^2x \left[-\frac{A}{2} \|\mathbf{Q}\|^2 + \frac{B}{4} \|\mathbf{Q}\|^4 + \frac{K}{2} \|\nabla \mathbf{Q}\|^2 \right] , \quad (\text{S3})$$

and $\|\mathbf{Q}\|^2 = Q_{ij}Q_{ij}$, $\|\nabla \mathbf{Q}\|^2 = \partial_k Q_{ij} \partial_k Q_{ij}$ (summation over repeated indices implied). We consider the relaxation in the cellular shape to be much faster than the flow (cell motion) time scale, allowing us to approximate the nematic texture, \mathbf{Q} to be always in a local equilibrium (dependent on boundary conditions). Functional minimisation of free energy in equation (S3) with respect to Q_{ij} results in non-linear PDE for \mathbf{Q} :

$$0 = -A Q_{ij} + B Q_{ij} \|\mathbf{Q}\|^2 - K \nabla^2 Q_{ij} . \quad (\text{S4})$$

The dynamic and kinematic boundary conditions on the flow are ($i = 1, 2$):

$$[(p_i^{\text{ext}} - p) \mathbf{n} + (2\eta \mathbf{D} + \alpha \mathbf{Q}) \cdot \mathbf{n}]|_{R_i} = \gamma(R_i) \kappa_i \mathbf{n} , \quad (\text{S5})$$

$$v_r|_{R_i} = \dot{R}_i + \frac{v_\theta|_{R_i}}{R_i} R_i' . \quad (\text{S6})$$

$D_{ij} = \frac{1}{2}(\partial_i v_j + \partial_j v_i)$ is the strain rate and p_i^{ext} is the pressure in the external fluid pressure in contact with the i^{th} free surface (see Fig. 1c). The effect of commonly observed actin-based mechanisms in re-epithelialisation (e.g. actin ‘purse-strings’, lamellopodia, filopodia) may be modelled by specifying the functional form of effective surface tension, $\gamma(R_i)$. Since here we are interested in the effect of activity in the bulk tissue on closure, we take $\gamma(R_i) = \gamma$, a constant for simplicity. We take parallel anchoring conditions on \mathbf{Q} at the inner boundary:

$$\begin{aligned} Q_{xx}|_{R_1} &= S_1 \frac{\cos 2\theta [(R_1')^2 - R_1^2] - 2R_1' R_1 \sin 2\theta}{R_1^2 + (R_1')^2} , \\ Q_{xy}|_{R_1} &= S_1 \frac{\sin 2\theta [(R_1')^2 - R_1^2] + 2R_1' R_1 \cos 2\theta}{R_1^2 + (R_1')^2} , \end{aligned} \quad (\text{S7a})$$

and x -axis alignment at the outer boundary:

$$Q_{xx}|_{R_2} = S_2, Q_{xy}|_{R_2} = 0. \quad (\text{S8})$$

S_i denotes the scalar nematic order parameter on the i^{th} boundary, $S_i = 0 \Rightarrow$ isotropic cells.

Non-Dimensionalisation

We non-dimensionalise by introducing length, time and pressure scales, and units for \mathbf{Q} : $\mathbf{r} \rightarrow L\mathbf{r}, t \rightarrow Tt, p \rightarrow \Pi p, \mathbf{Q} \rightarrow Q_0\mathbf{Q}$, choosing:

$$L = \sqrt{\frac{\eta}{\Gamma}}, \quad T = \frac{\eta}{\Pi}, \quad \Pi = \frac{\gamma}{L}, \quad Q_0 = \sqrt{\frac{A}{2B}}. \quad (\text{S9})$$

The non-dimensional equations of motion,

$$0 = \nabla \cdot \mathbf{v}, \quad (\text{S10a})$$

$$0 = -\nabla p + \nabla^2 \mathbf{v} - \mathbf{v} + \epsilon_\alpha (\nabla \cdot \mathbf{Q}), \quad (\text{S10b})$$

$$0 = \Lambda^2 Q_{ij} [(Q_{xx}^2 + Q_{xy}^2) - 1] - 2\nabla^2 Q_{ij}, \quad (\text{S10c})$$

now contain two dimensionless parameters, $\epsilon_\alpha = \alpha Q_0 / \Pi$ and $\Lambda = L / \ell_Q$. ϵ_α determines the strength of bulk active stresses relative to other passive stresses and Λ is the ratio of flow ($L^2 = \eta / \Gamma$) to nematic length scales ($\ell_Q^2 = K / 2A$) and governs the persistence of active stresses into the bulk. $1/\Lambda$ gives a proxy for the nematic length scale in the system.

Perturbation Parameter

Our experimental wounds are approximately circular throughout closure, so we choose to expand around circular free boundaries, using the non-dimensionalised activity $\epsilon_\alpha = \alpha Q_0 / \Pi$ as the perturbation parameter:

$$R_i(\theta, t) = R_i^0(t) + \epsilon_\alpha R_i^1(\theta, t) \quad (\text{S11a})$$

$$\mathbf{v} = \mathbf{v}^0 + \epsilon_\alpha \mathbf{v}^1 + \dots \quad (\text{S11b})$$

$$p = p^0 + \epsilon_\alpha p^1 + \dots \quad (\text{S11c})$$

$$\mathbf{Q} = \mathbf{Q}^0 + \epsilon_\alpha \mathbf{Q}^1 + \dots \quad (\text{S11d})$$

In this way, the leading order problem is that of a passive droplet in an axisymmetric annulus of with inner and outer radii $R_1^0(t), R_2^0(t)$. Further, the first order contributions to the flow only ‘see’ leading order contributions from the nematic driving. This can be seen by substituting the expansion into the non-dimensionalised Stokes equation:

$$0 = -\nabla p^0 + \nabla^2 \mathbf{v}^0 - \mathbf{v}^0 + \epsilon_\alpha [-\nabla p^1 + \nabla^2 \mathbf{v}^1 - \mathbf{v}^1 + \nabla \cdot \mathbf{Q}^0] + \mathcal{O}(\epsilon_\alpha^2).$$

This expansion approximation should provide accurate qualitative predictions provided the non-circularity $\epsilon_\alpha R_i^1 / R_i^0$ remains small, which since we consider circular initial conditions, will be satisfied for short times immediately following wounding. This is appropriate for a continuum model for re-epithelialisation, as we expect that as the wound size approaches the scale of individual cells, other mechanisms will become important.

CALCULATIONAL DETAILS

Boundary Conditions at $\mathcal{O}(1)$

Substituting expansions (S11), we obtain boundary conditions for each order in ϵ_α . At $\mathcal{O}(1)$, the normal and tangential components of the dynamic boundary conditions on each boundary read:

$$\begin{aligned} -\frac{\mu_i}{R_i^0} &= [p_i^{\text{ext}} - p^0 + 2\partial_r v_r^0] \Big|_{R_i^0}, \\ 0 &= \left[\frac{\partial_\theta v_r^0}{R_i^0} + \partial_r v_\theta^0 - \frac{v_\theta^0}{R_i^0} \right] \Big|_{R_i^0}, \end{aligned} \quad (\text{S12})$$

where μ_i is an index $\mu_1 = -1$ for the inner boundary, $\mu_2 = +1$ for the outer boundary. This is included to ensure the relative directions of surface tension and the outward normals are correctly accounted for – on the inner boundary, surface tension points in the *same* direction as the outward normal, whereas surface tension points in the *opposite* direction to the outward normal on the outer boundary. The kinematic boundary condition at $\mathcal{O}(1)$ reads

$$v_r^0|_{R_i^0} = \dot{R}_i^0. \quad (\text{S13})$$

The boundary conditions on the nematic texture at $\mathcal{O}(1)$ are

$$Q_{xx}^0|_{R_1^0} = -\beta_1 \cos 2\theta, \quad (\text{S14a})$$

$$Q_{xy}^0|_{R_1^0} = -\beta_1 \sin 2\theta, \quad (\text{S14b})$$

$$Q_{xx}^0|_{R_2^0} = \beta_2, \quad (\text{S14c})$$

$$Q_{xy}^0|_{R_2^0} = 0, \quad (\text{S14d})$$

where $\beta_i = S_i/(2Q_0)$ is the rescaled nematic scalar order at the i^{th} boundary. The forms for the boundary conditions at $\mathcal{O}(\epsilon_\alpha)$ are more complicated, as they require one to a) replace each dynamical field with its expansion in ϵ_α and b) Taylor expand each term in the first argument around radius R_i^0 . That is, $v_r|_{R_i} = [v_r^0 + \epsilon_\alpha v_r^1 + \dots]|_{R_i} = [v_r^0 + \epsilon_\alpha (R_i^1 \partial_r v_r^0 + v_r^1) + \dots]|_{R_i^0}$. Therefore, we momentarily postpone our statement of the boundary conditions on the flow at $\mathcal{O}(\epsilon_\alpha)$.

Nematic Texture at $\mathcal{O}(1)$

Equation (S10c) is a non-linear PDE, which we linearise by expanding around the homogeneous ordered state aligning along the x -axis:

$$\mathbf{Q}^0 = \begin{pmatrix} 1 + q_1 & q_2 \\ q_2 & -1 - q_1 \end{pmatrix}.$$

Substituting into equation (S10c) and ignoring terms $\mathcal{O}(q^2, p^2)$, we obtain two linear PDEs for q_1, q_2 :

$$\Rightarrow \quad \nabla^2 q_1 - \Lambda^2 q_1 \approx 0, \quad \nabla^2 q_2 \approx 0, \quad (\text{S15})$$

which will provide a good approximation to the nematic field provided $|q_1|, |q_2| \ll 1$. Solutions to equations (S15) are sums of modified Bessel functions and powers of r respectively. Substituting into the boundary conditions (S14), and solving the resulting linear system for unknown constants, we find:

$$q_1(r, \theta, t) = e_0 K_0(\Lambda r) + f_0 I_0(\Lambda r) + \cos 2\theta [e_2 K_2(\Lambda r) + g_2 I_2(\Lambda r)], \quad (\text{S16a})$$

$$q_2(r, \theta, t) = \sin 2\theta \left[\frac{b_2}{r^2} + d_2 r^2 \right], \quad (\text{S16b})$$

where $e_0, f_0, b_2, d_2, e_2, g_2$ are all known, but complicated, functions of R_1, R_2, Λ :

$$e_0 = \frac{(1 - \beta_2) I_0(\Lambda R_1^0) - I_0(\Lambda R_2^0)}{I_0(\Lambda R_2^0) K_0(\Lambda R_1^0) - I_0(\Lambda R_1^0) K_0(\Lambda R_2^0)}, \quad (\text{S17a})$$

$$f_0 = -\frac{(1 - \beta_2) K_0(\Lambda R_1^0) - K_0(\Lambda R_2^0)}{I_0(\Lambda R_2^0) K_0(\Lambda R_1^0) - I_0(\Lambda R_1^0) K_0(\Lambda R_2^0)}, \quad (\text{S17b})$$

$$b_2 = \frac{\beta_1 (R_1^0)^2 (R_2^0)^4}{(R_1^0)^4 - (R_2^0)^4}, \quad (\text{S17c})$$

$$d_2 = -\frac{\beta_1 (R_1^0)^2}{(R_1^0)^4 - (R_2^0)^4}, \quad (\text{S17d})$$

$$e_2 = -\frac{\beta_1 I_2 (\Lambda R_2^0)}{I_2 (\Lambda R_2^0) K_2 (\Lambda R_1^0) - I_2 (\Lambda R_1^0) K_2 (\Lambda R_2^0)}, \quad (\text{S17e})$$

$$g_2 = \frac{\beta_1 K_2 (\Lambda R_2^0)}{I_2 (\Lambda R_2^0) K_2 (\Lambda R_1^0) - I_2 (\Lambda R_1^0) K_2 (\Lambda R_2^0)}. \quad (\text{S17f})$$

The form of the driving term appearing in the Stokes eqn. at $\mathcal{O}(\epsilon_\alpha)$ is then determined by transforming components of \mathbf{Q}^0 from the Cartesian to polar bases, and taking the divergence in polar coordinates. The symmetry of the tensorial nematic order parameter means that components of \mathbf{Q}^0 in the Cartesian basis are transformed to the polar basis simply as:

$$\begin{pmatrix} Q_{rr} & Q_{r\theta} \\ Q_{r\theta} & -Q_{rr} \end{pmatrix} = \begin{pmatrix} \cos 2\theta & \sin 2\theta \\ -\sin 2\theta & \cos 2\theta \end{pmatrix} \begin{pmatrix} Q_{xx} & Q_{xy} \\ Q_{xy} & -Q_{xx} \end{pmatrix}, \quad (\text{S18})$$

where θ is the polar coordinate angle. The full form of the driving at $\mathcal{O}(\epsilon_\alpha)$ is then:

$$\begin{aligned} \nabla \cdot \mathbf{Q}^0 = & -[G_2(r) \sin(2\theta) + G_4(r) \sin(4\theta)] \hat{e}_\theta \\ & + [G_0(r) + G_2(r) \cos(2\theta) + G_4(r) \cos(4\theta)] \hat{e}_r, \end{aligned} \quad (\text{S19})$$

where

$$G_0(r) = +2d_2 r - \frac{1}{2} e_2 \Lambda K_1(r\Lambda) + \frac{1}{2} g_2 \Lambda I_1(r\Lambda), \quad (\text{S20a})$$

$$G_2(r) = -\Lambda e_0 K_1(r\Lambda) + \Lambda f_0 I_1(r\Lambda), \quad (\text{S20b})$$

$$G_4(r) = \frac{2b_2}{r^3} - \frac{1}{2} e_2 \Lambda K_3(r\Lambda) + \frac{1}{2} g_2 \Lambda I_3(r\Lambda). \quad (\text{S20c})$$

And for reasons that will become apparent later, we also have:

$$\begin{aligned} [\nabla \times (\nabla \cdot \mathbf{Q}^0)]_z = & -\Lambda^2 \sin 2\theta [f_0 I_2(\Lambda r) + e_0 K_2(\Lambda r)] \\ & - \sin 4\theta \left[\Lambda^2 [e_2 K_4(\Lambda r) + g_2 I_4(\Lambda r)] - \frac{12b_2}{r^4} \right]. \end{aligned} \quad (\text{S21})$$

Flow at $\mathcal{O}(1)$

The velocity field at can be determined straightforwardly in the passive problem by invoking a symmetry argument and integrating the incompressibility condition. However, once axisymmetry no longer applies, we will not be able to assume radial flow. Therefore, we spend a moment considering solutions to the Stokes equation of the form:

$$\nabla p = \nabla^2 \mathbf{v} - \mathbf{v}. \quad (\text{S22})$$

The solutions to the Stokes equation at $\mathcal{O}(\epsilon_\alpha)$ will then share the same complementary function, with an additional particular integral arising from nematic driving. We momentarily drop superscripts ⁰ for clarity. It will be convenient to use the stream function, defined as $\mathbf{v} = \nabla \times (\psi \hat{e}_z)$, where ψ is the stream function and \hat{e}_z is the unit vector pointing out of the plane. Taking the curl of equation (S22) and replacing $\nabla \times \mathbf{v} = \omega_z \hat{e}_z = -\nabla^2 \psi \hat{e}_z$ (where ω_z is the vorticity component in the z -direction), we obtain a modified biharmonic equation:

$$0 = \nabla^4 \psi - \nabla^2 \psi. \quad (\text{S23})$$

Solutions to equation (S23) may be categorised into four apparently distinct families, those for which:

1. $\nabla^2 \psi_1 = 0$,
2. $\nabla^2 \psi_2 - \psi_2 = 0$,

3. $\nabla^2 \psi_3 = \phi_1$ where $\nabla^2 \phi_1 - \phi_1 = 0$,
4. $\nabla^2 \psi_4 - \psi_4 = \phi_2$ where $\nabla^2 \phi_2 = 0$.

Let the space of solutions to the Laplace and Helmholtz equations be denoted as L and H respectively. Then clearly $\psi_1 \in L$, $\psi_2 \in H$. ψ_3 has complementary functions $\psi_3^{\text{CF}} \in L$ and particular integral $\psi_3^{\text{PI}} = \phi_1 \in H$. Finally, ψ_4 has complementary functions $\psi_4^{\text{CF}} \in H$ and particular integral $\psi_4^{\text{PI}} = -\phi_2 \in L$. Therefore, all together, we have a complementary function which is a sum of ‘Laplace-like’ and ‘Helmholtz-like’ terms:

$$\psi^{\text{CF}} = \psi^L + \psi^H, \quad \text{where} \quad \nabla^2 \psi^L = 0, \quad \nabla^2 \psi^H - \psi^H = 0, \quad (\text{S24})$$

or explicitly, only considering terms that generate a velocity field periodic in θ

$$\begin{aligned} \psi^{\text{CF}} = & A_0 \log r + C_0 \theta + \sum_{n=1}^{\infty} r^{-n} (A_n \cos n\theta + B_n \sin n\theta) + r^n (C_n \cos n\theta + D_n \sin n\theta) \\ & + E_0 K_0(r) + G_0 I_0(r) + \sum_{n=1}^{\infty} K_n(r) (E_n \cos n\theta + F_n \sin n\theta) + I_n(r) (G_n \cos n\theta + H_n \sin n\theta), \end{aligned} \quad (\text{S25})$$

where the constants $\{A_0, C_0, \dots, H_n\}$ are all constants with respect to position and $I_n(r), K_n(r)$ are modified Bessel functions of the first and second kind respectively [S2]. Automatically, we fix the constants $E_0 = G_0 = 0$, by looking for a solution with zero circulation $\Omega = \int_{\text{fluid}} \omega_z dS = 0$. We also require $A_0 = 0$ to give a pressure that is periodic in θ . To see this, substitute the velocity back into the Stokes equation:

$$\begin{aligned} \nabla p = \nabla^2 \mathbf{v} - \mathbf{v} &= \nabla^2 [\nabla \times (\psi \hat{e}_z)] - \nabla \times (\psi \hat{e}_z) = \nabla \times [(\nabla^2 \psi - \psi) \hat{e}_z] = -\nabla \times (\psi^L \hat{e}_z) \\ &= \hat{e}_r \left[-\frac{C_0}{r} + \dots \right] + \hat{e}_\theta \left[+\frac{A_0}{r} + \dots \right], \end{aligned}$$

and integrating the tangential component of this equation: $\frac{1}{r} \partial_\theta p = \frac{A_0}{r} + \dots \Rightarrow p = A_0 \theta + \dots$ which is aperiodic in θ , and hence excluded. Physically relevant solutions to the homogeneous Stokes equation are then of the form:

$$\begin{aligned} \psi^{\text{CF}} = & C_0 \theta + \sum_{n=1}^{\infty} r^{-n} (A_n \cos n\theta + B_n \sin n\theta) + r^n (C_n \cos n\theta + D_n \sin n\theta) \\ & + \sum_{n=1}^{\infty} K_n(r) (E_n \cos n\theta + F_n \sin n\theta) + I_n(r) (G_n \cos n\theta + H_n \sin n\theta), \end{aligned} \quad (\text{S26a})$$

$$p^{\text{CF}} = D_0 - C_0 \log r + \sum_{n=1}^{\infty} r^{-n} (-A_n \sin n\theta + B_n \cos n\theta) + r^n (C_n \sin n\theta - D_n \cos n\theta). \quad (\text{S26b})$$

The remaining constants are found by substituting the stream function and pressure into each component of the dynamic boundary conditions at each boundary, comparing coefficients of trigonometric functions and solving the resulting linear system. In practice, this step is performed using Mathematica, the code for which we have made available at <https://github.com/andra516/dynamicsOfWoundClosure>. At $\mathcal{O}(1)$ we find (reinstating superscripts):

$$\psi^0 = \tilde{c}_0 \theta, \quad p^0 = \tilde{d}_0 - \tilde{c}_0 \log r \quad \Rightarrow \quad \mathbf{v}^0 = \frac{\tilde{c}_0}{r} \hat{e}_r, \quad (\text{S27})$$

where

$$\tilde{c}_0 = -\frac{R_1^0 R_2^0 (R_2^0 + R_1^0) + P(R_1^0 R_2^0)^2}{2[(R_2^0)^2 - (R_1^0)^2] + (R_1^0 R_2^0)^2 \log \frac{R_2^0}{R_1^0}}. \quad (\text{S28})$$

Finally, the time evolution of each boundary is determined by substituting the velocity field into the kinematic boundary condition (S13):

$$\dot{R}_1^0 = \frac{\tilde{c}_0}{R_1^0}, \quad \dot{R}_2^0 = \frac{\tilde{c}_0}{R_2^0},$$

and hence:

$$\dot{R}_1^0 = -\frac{R_2^0 (R_2^0 + R_1^0) + P R_1^0 (R_2^0)^2}{2 [(R_2^0)^2 - (R_1^0)^2] + (R_1^0 R_2^0)^2 \log \frac{R_2^0}{R_1^0}}, \quad (\text{S29a})$$

and a similar equation for \dot{R}_2^0 :

$$\dot{R}_2^0 = -\frac{R_1^0 (R_2^0 + R_1^0) + P R_2^0 (R_1^0)^2}{2 [(R_2^0)^2 - (R_1^0)^2] + (R_1^0 R_2^0)^2 \log \frac{R_2^0}{R_1^0}}. \quad (\text{S29b})$$

In practice, whenever numerically integrating ODEs for the shape modes (such as those in equations (S29)), unless otherwise stated, we take $R_1^0(t=0) = 1$, $R_2^0(t=0) = 20$. This ensures the outer boundary remains approximately stationary throughout closure, $\dot{R}_2^0/R_2^0 \stackrel{\text{incomp.}}{=} \dot{R}_1^0 R_1^0 / (R_2^0)^2 \ll 1$.

Boundary Conditions at $\mathcal{O}(\epsilon_\alpha)$

Having solved the passive problem, we now state the boundary conditions on the flow at $\mathcal{O}(\epsilon_\alpha)$. Expanding the full boundary conditions and substituting the leading order flow and nematic texture, the $\mathcal{O}(\epsilon_\alpha)$ DBCs at the inner boundary read:

$$-\frac{R_1^1 + (R_1^1)''}{(R_1^0)^2} = \left[\frac{\tilde{c}_0 R_1^1}{R_1^0} + \frac{4\tilde{c}_0 R_1^1}{(R_1^0)^3} - p^1 + 2\partial_r v_r^1 - \beta_1 \right] \Big|_{R_1^0}, \quad (\text{S30a})$$

$$0 = \left[-\frac{4\tilde{c}_0 (R_1^1)'}{(R_1^0)^3} + \frac{\partial_\theta v_r^1}{R_1^0} - \frac{v_\theta^1}{R_1^0} + \partial_r v_\theta^1 \right] \Big|_{R_1^0}, \quad (\text{S30b})$$

and at the outer:

$$\frac{R_2^1 + (R_2^1)''}{(R_2^0)^2} = \left[\frac{\tilde{c}_0 R_2^1}{R_2^0} + \frac{4\tilde{c}_0 R_2^1}{(R_2^0)^3} - p^1 + 2\partial_r v_r^1 + \beta_2 \cos 2\theta \right] \Big|_{R_2^0}, \quad (\text{S30c})$$

$$0 = \left[-\frac{4\tilde{c}_0 (R_2^1)'}{(R_2^0)^3} + \frac{\partial_\theta v_r^1}{R_2^0} + \partial_r v_\theta^1 - \frac{v_\theta^1}{R_2^0} - \beta_2 \sin 2\theta \right] \Big|_{R_2^0}, \quad (\text{S30d})$$

where $(\cdot)'$ denotes differentiation with respect to θ . The kinematic boundary condition on each boundary at $\mathcal{O}(\epsilon_\alpha)$ reads:

$$v_r^1|_{R_i^0} = \dot{R}_i^1 + \frac{\tilde{c}_0 R_i^1}{(R_i^0)^2}. \quad (\text{S31})$$

Flow at $\mathcal{O}(\epsilon_\alpha)$

The Stokes equation at $\mathcal{O}(\epsilon_\alpha)$ is similar to that of the unperturbed problem, with additional driving from $(\nabla \cdot \mathbf{Q}^0)$. Therefore, the complementary functions for the stream function and pressure will be given by equations (S26), with additional particular integrals coming from the driving. Taking the curl of the Stokes equation at $\mathcal{O}(\epsilon_\alpha)$ and considering the z component, the stream function satisfies:

$$[\nabla \times (\nabla \cdot \mathbf{Q}^0)]_z = \nabla^4 \psi^1 - \nabla^2 \psi^1, \quad (\text{S32})$$

where (see eqn. (S21))

$$\begin{aligned} [\nabla \times (\nabla \cdot \mathbf{Q}^0)]_z &= -\Lambda^2 \sin 2\theta [f_0 I_2(\Lambda r) + e_0 K_2(\Lambda r)] \\ &\quad - \sin 4\theta \left[\Lambda^2 [e_2 K_4(\Lambda r) + g_2 I_4(\Lambda r)] - \frac{12b_2}{r^4} \right]. \end{aligned}$$

The pressure satisfies:

$$\nabla^2 p^1 = \nabla \cdot (\nabla \cdot \mathbf{Q}^0). \quad (\text{S33})$$

Therefore, together with complementary functions given by equations (S26), we also have particular integrals:

$$\psi_{\text{PI}}^1 = \frac{[e_0 K_2(\Lambda r) + f_0 I_2(\Lambda r)]}{1 - \Lambda^2} \sin 2\theta + \left[\frac{b_2}{r^2} + \frac{e_2 K_4(\Lambda r) + g_2 I_4(\Lambda r)}{2(1 - \Lambda^2)} \right] \sin 4\theta, \quad (\text{S34a})$$

$$\begin{aligned} p_{\text{PI}}^1 = & d_2 r^2 + \frac{e_2}{2} K_0(\Lambda r) + \frac{g_2}{2} I_0(\Lambda r) + \cos 2\theta [e_0 K_2(\Lambda r) + f_0 I_2(\Lambda r)] \\ & + \cos 4\theta \left[\frac{12b_2}{r^4} + \frac{b_2}{r^2} + \frac{e_2}{2} K_4(\Lambda r) + \frac{g_2}{2} I_4(\Lambda r) \right]. \end{aligned} \quad (\text{S34b})$$

Substituting into the dynamic boundary conditions at each boundary and equating coefficients of trigonometric functions, we have to solve the following linear problems for the constants in the complementary functions (equations (S26)):

$$\begin{pmatrix} \mathcal{A}_{11}^0 & \mathcal{A}_{12}^0 \\ \mathcal{A}_{21}^0 & \mathcal{A}_{22}^0 \end{pmatrix} \begin{pmatrix} \tilde{c}_0 \\ D_0 \end{pmatrix} = \begin{pmatrix} \mathcal{V}_1^0 \\ \mathcal{V}_2^0 \end{pmatrix}, \quad (\text{S35a})$$

where

$$\begin{aligned} \mathcal{A}_{11}^0 &= \frac{2}{(R_1^0)^2} - \log(R_1^0), \\ \mathcal{A}_{12}^0 &= 1, \\ \mathcal{A}_{21}^0 &= \frac{2}{(R_2^0)^2} - \log(R_2^0), \\ \mathcal{A}_{22}^0 &= 1, \end{aligned}$$

and

$$\begin{aligned} \mathcal{V}_1^0 &= \frac{\tilde{c}_0 \xi_1^0}{R_1^0} + \frac{4\tilde{c}_0 \xi_1^0}{(R_1^0)^3} - d_2 (R_1^0)^2 - \frac{1}{2} e_2 K_0(\Lambda R_1^0) - \frac{1}{2} g_2 I_0(\Lambda R_1^0) + \frac{\xi_1^0}{(R_1^0)^2} - \beta_1, \\ \mathcal{V}_2^0 &= \frac{\xi_2^0 (\tilde{c}_0 ((R_2^0)^2 + 4) - R_2^0)}{(R_2^0)^3} - d_2 (R_2^0)^2 - \frac{1}{2} e_2 K_0(\Lambda R_2^0) - \frac{1}{2} g_2 I_0(\Lambda R_2^0). \end{aligned}$$

$$\begin{pmatrix} \mathcal{P}_{11}^2 & \mathcal{P}_{12}^2 & \mathcal{P}_{13}^2 & \mathcal{P}_{14}^2 \\ \mathcal{P}_{11}^2 & \mathcal{P}_{12}^2 & \mathcal{P}_{13}^2 & \mathcal{P}_{14}^2 \\ \mathcal{P}_{11}^2 & \mathcal{P}_{12}^2 & \mathcal{P}_{13}^2 & \mathcal{P}_{14}^2 \\ \mathcal{P}_{11}^2 & \mathcal{P}_{12}^2 & \mathcal{P}_{13}^2 & \mathcal{P}_{14}^2 \end{pmatrix} \begin{pmatrix} A_2 \\ C_2 \\ E_2 \\ G_2 \end{pmatrix} = \begin{pmatrix} \mathcal{W}_1^2 \\ \mathcal{W}_2^2 \\ \mathcal{W}_3^2 \\ \mathcal{W}_4^2 \end{pmatrix}, \quad (\text{S35b})$$

where

$$\begin{aligned}
\mathcal{P}_{11}^2 &= -\left(R_1^0\right)^2 - 12, \\
\mathcal{P}_{12}^2 &= R_1^0 \left(\left(R_1^0\right)^5 + 4 \left(R_1^0\right)^3 \right), \\
\mathcal{P}_{13}^2 &= -4 \left(R_1^0\right)^2 \left(3K_2 \left(R_1^0\right) + R_1^0 K_1 \left(R_1^0\right) \right), \\
\mathcal{P}_{14}^2 &= 4 \left(R_1^0\right)^2 \left(R_1^0 I_1 \left(R_1^0\right) - 3I_2 \left(R_1^0\right) \right), \\
\mathcal{P}_{21}^2 &= \frac{12}{\left(R_1^0\right)^4}, \\
\mathcal{P}_{22}^2 &= 4, \\
\mathcal{P}_{23}^2 &= \frac{2K_1 \left(R_1^0\right)}{R_1^0} + K_2 \left(R_1^0\right) + \frac{12K_2 \left(R_1^0\right)}{\left(R_1^0\right)^2}, \\
\mathcal{P}_{24}^2 &= -\frac{2I_1 \left(R_1^0\right)}{R_1^0} + I_2 \left(R_1^0\right) + \frac{12I_2 \left(R_1^0\right)}{\left(R_1^0\right)^2}, \\
\mathcal{P}_{31}^2 &= -\left(R_2^0\right)^2 - 12, \\
\mathcal{P}_{32}^2 &= R_2^0 \left(\left(R_2^0\right)^5 + 4 \left(R_2^0\right)^3 \right), \\
\mathcal{P}_{33}^2 &= -4 \left(R_2^0\right)^2 \left(3K_2 \left(R_2^0\right) + R_2^0 K_1 \left(R_2^0\right) \right), \\
\mathcal{P}_{34}^2 &= 4 \left(R_2^0\right)^2 \left(R_2^0 I_1 \left(R_2^0\right) - 3I_2 \left(R_2^0\right) \right), \\
\mathcal{P}_{41}^2 &= \frac{12}{\left(R_2^0\right)^4}, \\
\mathcal{P}_{42}^2 &= 4, \\
\mathcal{P}_{43}^2 &= \frac{2K_1 \left(R_2^0\right)}{R_2^0} + K_2 \left(R_2^0\right) + \frac{12K_2 \left(R_2^0\right)}{\left(R_2^0\right)^2}, \\
\mathcal{P}_{44}^2 &= -\frac{2I_1 \left(R_2^0\right)}{R_2^0} + I_2 \left(R_2^0\right) + \frac{12I_2 \left(R_2^0\right)}{\left(R_2^0\right)^2},
\end{aligned}$$

and

$$\begin{aligned}
\mathcal{W}_1^2 &= R_1^0 \eta_1^2 \left(\tilde{c}_0 \left(\left(R_1^0\right)^2 + 4 \right) - 3R_1^0 \right), \\
\mathcal{W}_2^2 &= -\frac{8\tilde{c}_0 \eta_1^2}{\left(R_1^0\right)^3}, \\
\mathcal{W}_3^2 &= R_2^0 \eta_2^2 \left(\tilde{c}_0 \left(\left(R_2^0\right)^2 + 4 \right) + 3R_2^0 \right), \\
\mathcal{W}_4^2 &= -\frac{8\tilde{c}_0 \eta_2^2}{\left(R_2^0\right)^3}.
\end{aligned}$$

$$\begin{pmatrix} \mathcal{A}_{11}^2 & \mathcal{A}_{12}^2 & \mathcal{A}_{13}^2 & \mathcal{A}_{14}^2 \\ \mathcal{A}_{11}^2 & \mathcal{A}_{12}^2 & \mathcal{A}_{13}^2 & \mathcal{A}_{14}^2 \\ \mathcal{A}_{11}^2 & \mathcal{A}_{12}^2 & \mathcal{A}_{13}^2 & \mathcal{A}_{14}^2 \\ \mathcal{A}_{11}^2 & \mathcal{A}_{12}^2 & \mathcal{A}_{13}^2 & \mathcal{A}_{14}^2 \end{pmatrix} \begin{pmatrix} B_2 \\ D_2 \\ F_2 \\ H_2 \end{pmatrix} = \begin{pmatrix} \mathcal{V}_1^2 \\ \mathcal{V}_2^2 \\ \mathcal{V}_3^2 \\ \mathcal{V}_4^2 \end{pmatrix}, \quad (\text{S35c})$$

where

$$\begin{aligned}
\mathcal{A}_{11}^2 &= -\frac{(\Lambda^2 - 1)((R_1^0)^2 + 12)}{R_1^0}, \\
\mathcal{A}_{12}^2 &= -((\Lambda^2 - 1)(-(R_1^0)^5 - 4(R_1^0)^3)), \\
\mathcal{A}_{13}^2 &= -4(\Lambda^2 - 1)R_1^0(3K_2(R_1^0) + R_1^0K_1(R_1^0)), \\
\mathcal{A}_{14}^2 &= 4(\Lambda^2 - 1)R_1^0(R_1^0I_1(R_1^0) - 3I_2(R_1^0)), \\
\mathcal{A}_{21}^2 &= -\frac{12(\Lambda^2 - 1)}{R_1^0}, \\
\mathcal{A}_{22}^2 &= -4(\Lambda^2 - 1)(R_1^0)^3, \\
\mathcal{A}_{23}^2 &= -((\Lambda^2 - 1)R_1^0((R_1^0)^2K_2(R_1^0) + 2R_1^0K_1(R_1^0) + 12K_2(R_1^0))), \\
\mathcal{A}_{24}^2 &= -((\Lambda^2 - 1)R_1^0((R_1^0)^2I_2(R_1^0) - 2R_1^0I_1(R_1^0) + 12I_2(R_1^0))), \\
\mathcal{A}_{31}^2 &= \frac{(\Lambda^2 - 1)((R_2^0)^2 + 12)}{R_2^0}, \\
\mathcal{A}_{32}^2 &= -((\Lambda^2 - 1)(R_2^0)^5) - 4(\Lambda^2 - 1)(R_2^0)^3, \\
\mathcal{A}_{33}^2 &= 4(\Lambda^2 - 1)R_2^0(3K_2(R_2^0) + R_2^0K_1(R_2^0)), \\
\mathcal{A}_{34}^2 &= -4(\Lambda^2 - 1)R_2^0(R_2^0I_1(R_2^0) - 3I_2(R_2^0)), \\
\mathcal{A}_{41}^2 &= -\frac{12(\Lambda^2 - 1)}{R_2^0}, \\
\mathcal{A}_{42}^2 &= -4(\Lambda^2 - 1)(R_2^0)^3, \\
\mathcal{A}_{43}^2 &= -((\Lambda^2 - 1)R_2^0((R_2^0)^2K_2(R_2^0) + 2R_2^0K_1(R_2^0) + 12K_2(R_2^0))), \\
\mathcal{A}_{44}^2 &= -((\Lambda^2 - 1)R_2^0((R_2^0)^2I_2(R_2^0) - 2R_2^0I_1(R_2^0) + 12I_2(R_2^0))),
\end{aligned}$$

and

$$\begin{aligned}
\mathcal{V}_1^2 &= -\tilde{c}_0\Lambda^2(R_1^0)^2\xi_1^2 + \tilde{c}_0(R_1^0)^2\xi_1^2 - 4\tilde{c}_0\Lambda^2\xi_1^2 + 4\tilde{c}_0\xi_1^2 + e_0\Lambda^2(R_1^0)^3K_2(\Lambda R_1^0) - e_0(R_1^0)^3K_2(\Lambda R_1^0) \\
&\quad - 4e_0\Lambda(R_1^0)^2K_1(\Lambda R_1^0) - 12e_0R_1^0K_2(\Lambda R_1^0) + f_0\Lambda^2(R_1^0)^3I_2(\Lambda R_1^0) - f_0(R_1^0)^3I_2(\Lambda R_1^0) \\
&\quad + 4f_0\Lambda(R_1^0)^2I_1(\Lambda R_1^0) - 12f_0R_1^0I_2(\Lambda R_1^0) + 3\Lambda^2R_1^0\xi_1^2 - 3R_1^0\xi_1^2, \\
\mathcal{V}_2^2 &= -8\tilde{c}_0\Lambda^2\xi_1^2 + 8\tilde{c}_0\xi_1^2 + e_0(-\Lambda^2)(R_1^0)^3K_2(\Lambda R_1^0) - 2e_0\Lambda(R_1^0)^2K_1(\Lambda R_1^0) - 12e_0R_1^0K_2(\Lambda R_1^0) \\
&\quad - f_0\Lambda^2(R_1^0)^3I_2(\Lambda R_1^0) + 2f_0\Lambda(R_1^0)^2I_1(\Lambda R_1^0) - 12f_0R_1^0I_2(\Lambda R_1^0), \\
\mathcal{V}_3^2 &= \tilde{c}_0\Lambda^2(R_2^0)^2\xi_2^2 - \tilde{c}_0(R_2^0)^2\xi_2^2 + 4\tilde{c}_0\Lambda^2\xi_2^2 - 4\tilde{c}_0\xi_2^2 + e_0(-\Lambda^2)(R_2^0)^3K_2(\Lambda R_2^0) + e_0(R_2^0)^3K_2(\Lambda R_2^0) \\
&\quad + 4e_0\Lambda(R_2^0)^2K_1(\Lambda R_2^0) + 12e_0R_2^0K_2(\Lambda R_2^0) - f_0\Lambda^2(R_2^0)^3I_2(\Lambda R_2^0) + f_0(R_2^0)^3I_2(\Lambda R_2^0) \\
&\quad - 4f_0\Lambda(R_2^0)^2I_1(\Lambda R_2^0) + 12f_0R_2^0I_2(\Lambda R_2^0) + \beta_2\Lambda^2(R_2^0)^3 - \beta_2(R_2^0)^3 + 3\Lambda^2R_2^0\xi_2^2 - 3R_2^0\xi_2^2, \\
\mathcal{V}_4^2 &= -8\tilde{c}_0\Lambda^2\xi_2^2 + 8\tilde{c}_0\xi_2^2 + e_0(-\Lambda^2)(R_2^0)^3K_2(\Lambda R_2^0) - 2e_0\Lambda(R_2^0)^2K_1(\Lambda R_2^0) - 12e_0R_2^0K_2(\Lambda R_2^0) \\
&\quad - f_0\Lambda^2(R_2^0)^3I_2(\Lambda R_2^0) + 2f_0\Lambda(R_2^0)^2I_1(\Lambda R_2^0) - 12f_0R_2^0I_2(\Lambda R_2^0) + \beta_2\Lambda^2(R_2^0)^3 - \beta_2(R_2^0)^3.
\end{aligned}$$

$$\begin{pmatrix} \mathcal{P}_{11}^4 & \mathcal{P}_{12}^4 & \mathcal{P}_{13}^4 & \mathcal{P}_{14}^4 \\ \mathcal{P}_{11}^4 & \mathcal{P}_{12}^4 & \mathcal{P}_{13}^4 & \mathcal{P}_{14}^4 \\ \mathcal{P}_{11}^4 & \mathcal{P}_{12}^4 & \mathcal{P}_{13}^4 & \mathcal{P}_{14}^4 \\ \mathcal{P}_{11}^4 & \mathcal{P}_{12}^4 & \mathcal{P}_{13}^4 & \mathcal{P}_{14}^4 \end{pmatrix} \begin{pmatrix} A_4 \\ C_4 \\ E_4 \\ G_4 \end{pmatrix} = \begin{pmatrix} \mathcal{W}_1^4 \\ \mathcal{W}_2^4 \\ \mathcal{W}_3^4 \\ \mathcal{W}_4^4 \end{pmatrix}, \quad (\text{S35d})$$

where

$$\begin{aligned}
\mathcal{P}_{11}^4 &= -\left(R_1^0\right)^2 - 40, \\
\mathcal{P}_{12}^4 &= \left(R_1^0\right)^3 \left(\left(R_1^0\right)^7 + 24\left(R_1^0\right)^5\right), \\
\mathcal{P}_{13}^4 &= -8\left(R_1^0\right)^4 \left(5K_4\left(R_1^0\right) + R_1^0 K_3\left(R_1^0\right)\right), \\
\mathcal{P}_{14}^4 &= 8\left(R_1^0\right)^4 \left(R_1^0 I_3\left(R_1^0\right) - 5I_4\left(R_1^0\right)\right), \\
\mathcal{P}_{21}^4 &= 40, \\
\mathcal{P}_{22}^4 &= 24\left(R_1^0\right)^8, \\
\mathcal{P}_{23}^4 &= \left(R_1^0\right)^4 \left(\left(R_1^0\right)^2 K_4\left(R_1^0\right) + 2R_1^0 K_3\left(R_1^0\right) + 40K_4\left(R_1^0\right)\right), \\
\mathcal{P}_{24}^4 &= \left(R_1^0\right)^4 \left(\left(R_1^0\right)^2 I_4\left(R_1^0\right) - 2R_1^0 I_3\left(R_1^0\right) + 40I_4\left(R_1^0\right)\right), \\
\mathcal{P}_{31}^4 &= -\left(R_2^0\right)^2 - 40, \\
\mathcal{P}_{32}^4 &= \left(R_2^0\right)^3 \left(\left(R_2^0\right)^7 + 24\left(R_2^0\right)^5\right), \\
\mathcal{P}_{33}^4 &= -8\left(R_2^0\right)^4 \left(5K_4\left(R_2^0\right) + R_2^0 K_3\left(R_2^0\right)\right), \\
\mathcal{P}_{34}^4 &= 8\left(R_2^0\right)^4 \left(R_2^0 I_3\left(R_2^0\right) - 5I_4\left(R_2^0\right)\right), \\
\mathcal{P}_{41}^4 &= 40, \\
\mathcal{P}_{42}^4 &= 24\left(R_2^0\right)^8, \\
\mathcal{P}_{43}^4 &= \left(R_2^0\right)^4 \left(\left(R_2^0\right)^2 K_4\left(R_2^0\right) + 2R_2^0 K_3\left(R_2^0\right) + 40K_4\left(R_2^0\right)\right), \\
\mathcal{P}_{44}^4 &= \left(R_2^0\right)^4 \left(\left(R_2^0\right)^2 I_4\left(R_2^0\right) - 2R_2^0 I_3\left(R_2^0\right) + 40I_4\left(R_2^0\right)\right),
\end{aligned}$$

and

$$\begin{aligned}
\mathcal{W}_1^4 &= \left(R_1^0\right)^3 \eta_1^4 \left(\tilde{c}_0 \left(\left(R_1^0\right)^2 + 4\right) - 15R_1^0\right), \\
\mathcal{W}_2^4 &= -16\tilde{c}_0 \left(R_1^0\right)^3 \eta_1^4, \\
\mathcal{W}_3^4 &= \left(R_2^0\right)^3 \eta_2^4 \left(\tilde{c}_0 \left(\left(R_2^0\right)^2 + 4\right) + 15R_2^0\right), \\
\mathcal{W}_4^4 &= -16\tilde{c}_0 \left(R_2^0\right)^3 \eta_2^4.
\end{aligned} \tag{S35e}$$

$$\begin{pmatrix} \mathcal{A}_{11}^4 & \mathcal{A}_{12}^4 & \mathcal{A}_{13}^4 & \mathcal{A}_{14}^4 \\ \mathcal{A}_{11}^4 & \mathcal{A}_{12}^4 & \mathcal{A}_{13}^4 & \mathcal{A}_{14}^4 \\ \mathcal{A}_{11}^4 & \mathcal{A}_{12}^4 & \mathcal{A}_{13}^4 & \mathcal{A}_{14}^4 \\ \mathcal{A}_{11}^4 & \mathcal{A}_{12}^4 & \mathcal{A}_{13}^4 & \mathcal{A}_{14}^4 \end{pmatrix} \begin{pmatrix} B_4 \\ D_4 \\ F_4 \\ H_4 \end{pmatrix} = \begin{pmatrix} \mathcal{V}_1^4 \\ \mathcal{V}_2^4 \\ \mathcal{V}_3^4 \\ \mathcal{V}_4^4 \end{pmatrix}, \tag{S35f}$$

where

$$\begin{aligned}
\mathcal{A}_{11}^4 &= \frac{(R_1^0)^2 + 40}{(R_1^0)^6}, \\
\mathcal{A}_{12}^4 &= - (R_1^0)^4 - 24 (R_1^0)^2, \\
\mathcal{A}_{13}^4 &= \frac{8 (5K_4 (R_1^0) + R_1^0 K_3 (R_1^0))}{(R_1^0)^2}, \\
\mathcal{A}_{14}^4 &= - \frac{8 (R_1^0 I_3 (R_1^0) - 5I_4 (R_1^0))}{(R_1^0)^2}, \\
\mathcal{A}_{21}^4 &= 80, \\
\mathcal{A}_{22}^4 &= 48 (R_1^0)^8, \\
\mathcal{A}_{23}^4 &= 2 (R_1^0)^4 ((R_1^0)^2 K_4 (R_1^0) + 2R_1^0 K_3 (R_1^0) + 40K_4 (R_1^0)), \\
\mathcal{A}_{24}^4 &= 2(R_1^0)^6 I_4(R_1^0) - 4(R_1^0)^5 I_3(R_1^0) + 80(R_1^0)^4 I_4(R_1^0), \\
\mathcal{A}_{31}^4 &= \frac{(R_2^0)^2 + 40}{(R_2^0)^6}, \\
\mathcal{A}_{32}^4 &= - (R_2^0)^4 - 24 (R_2^0)^2, \\
\mathcal{A}_{33}^4 &= \frac{8 (5K_4 (R_2^0) + R_2^0 K_3 (R_2^0))}{(R_2^0)^2}, \\
\mathcal{A}_{34}^4 &= - \frac{8 (R_2^0 I_3 (R_2^0) - 5I_4 (R_2^0))}{(R_2^0)^2}, \\
\mathcal{A}_{41}^4 &= 80, \\
\mathcal{A}_{42}^4 &= 48(R_2^0)^8, \\
\mathcal{A}_{43}^4 &= 2 (R_2^0)^4 ((R_2^0)^2 K_4 (R_2^0) + 2R_2^0 K_3 (R_2^0) + 40K_4 (R_2^0)), \\
\mathcal{A}_{44}^4 &= 2(R_2^0)^6 I_4(R_2^0) - 4(R_2^0)^5 I_3(R_2^0) + 80(R_2^0)^4 I_4(R_2^0),
\end{aligned}$$

and

$$\begin{aligned}
\mathcal{V}_1^4 &= -\frac{b_2}{(R_1^0)^2} - \frac{36b_2}{(R_1^0)^4} + \frac{\tilde{c}_0 \xi_1^4}{R_1^0} + \frac{4\tilde{c}_0 \xi_1^4}{(R_1^0)^3} - \frac{e_2 K_4 (\Lambda R_1^0)}{2} + \frac{4e_2 \Lambda K_3 (\Lambda R_1^0)}{(\Lambda^2 - 1)R_1^0} + \frac{20e_2 K_4 (\Lambda R_1^0)}{(\Lambda^2 - 1)(R_1^0)^2} \\
&\quad - \frac{g_2 I_4 (\Lambda R_1^0)}{2} - \frac{4g_2 \Lambda I_3 (\Lambda R_1^0)}{(\Lambda^2 - 1)R_1^0} + \frac{20g_2 I_4 (\Lambda R_1^0)}{(\Lambda^2 - 1)(R_1^0)^2} - \frac{15\xi_1^4}{(R_1^0)^2}, \\
\mathcal{V}_2^4 &= -48b_2 (R_1^0)^2 + 32\tilde{c}_0 (R_1^0)^3 \xi_1^4 + \frac{\Lambda^2 (R_1^0)^6}{\Lambda^2 - 1} (e_2 K_4 (\Lambda R_1^0) + g_2 I_4 (\Lambda R_1^0)) \\
&\quad + \frac{2\Lambda (R_1^0)^5}{\Lambda^2 - 1} (e_2 K_3 (\Lambda R_1^0) - g_2 I_3 (\Lambda R_1^0)) + \frac{40(R_1^0)^4}{\Lambda^2 - 1} (e_2 K_4 (\Lambda R_1^0) + g_2 I_4 (\Lambda R_1^0)), \\
\mathcal{V}_3^4 &= -\frac{b_2}{(R_2^0)^2} - \frac{36b_2}{(R_2^0)^4} + \frac{\tilde{c}_0 \xi_2^4}{R_2^0} + \frac{4\tilde{c}_0 \xi_2^4}{(R_2^0)^3} - \frac{e_2 K_4 (\Lambda R_2^0)}{2} + \frac{4e_2 \Lambda K_3 (\Lambda R_2^0)}{(\Lambda^2 - 1)R_2^0} + \frac{20e_2 K_4 (\Lambda R_2^0)}{(\Lambda^2 - 1)(R_2^0)^2} \\
&\quad - \frac{g_2 I_4 (\Lambda R_2^0)}{2} - \frac{4g_2 \Lambda I_3 (\Lambda R_2^0)}{(\Lambda^2 - 1)R_2^0} + \frac{20g_2 I_4 (\Lambda R_2^0)}{(\Lambda^2 - 1)(R_2^0)^2} - \frac{15\xi_2^4}{(R_2^0)^2}, \\
\mathcal{V}_4^4 &= -48b_2 (R_2^0)^2 + 32\tilde{c}_0 (R_2^0)^3 \xi_2^4 + \frac{\Lambda^2 (R_2^0)^6}{\Lambda^2 - 1} (e_2 K_4 (\Lambda R_2^0) + g_2 I_4 (\Lambda R_2^0)) \\
&\quad + \frac{2\Lambda (R_2^0)^5}{\Lambda^2 - 1} (e_2 K_3 (\Lambda R_2^0) - g_2 I_3 (\Lambda R_2^0)) + \frac{40(R_2^0)^4}{\Lambda^2 - 1} (e_2 K_4 (\Lambda R_2^0) + g_2 I_4 (\Lambda R_2^0)).
\end{aligned}$$

The exact form of constants $\{C_0, D_0, A_2, \dots\}$ are complicated and refer the reader to our code that solves the problem in full.

Finally, we substitute the velocity field into the KBCs at $\mathcal{O}(\epsilon_\alpha)$, equation (S31). Equating coefficients of trigonometric functions, we obtain ODEs for the shape mode amplitudes, ξ_i^n, η_i^n . These ODEs have complex dependencies

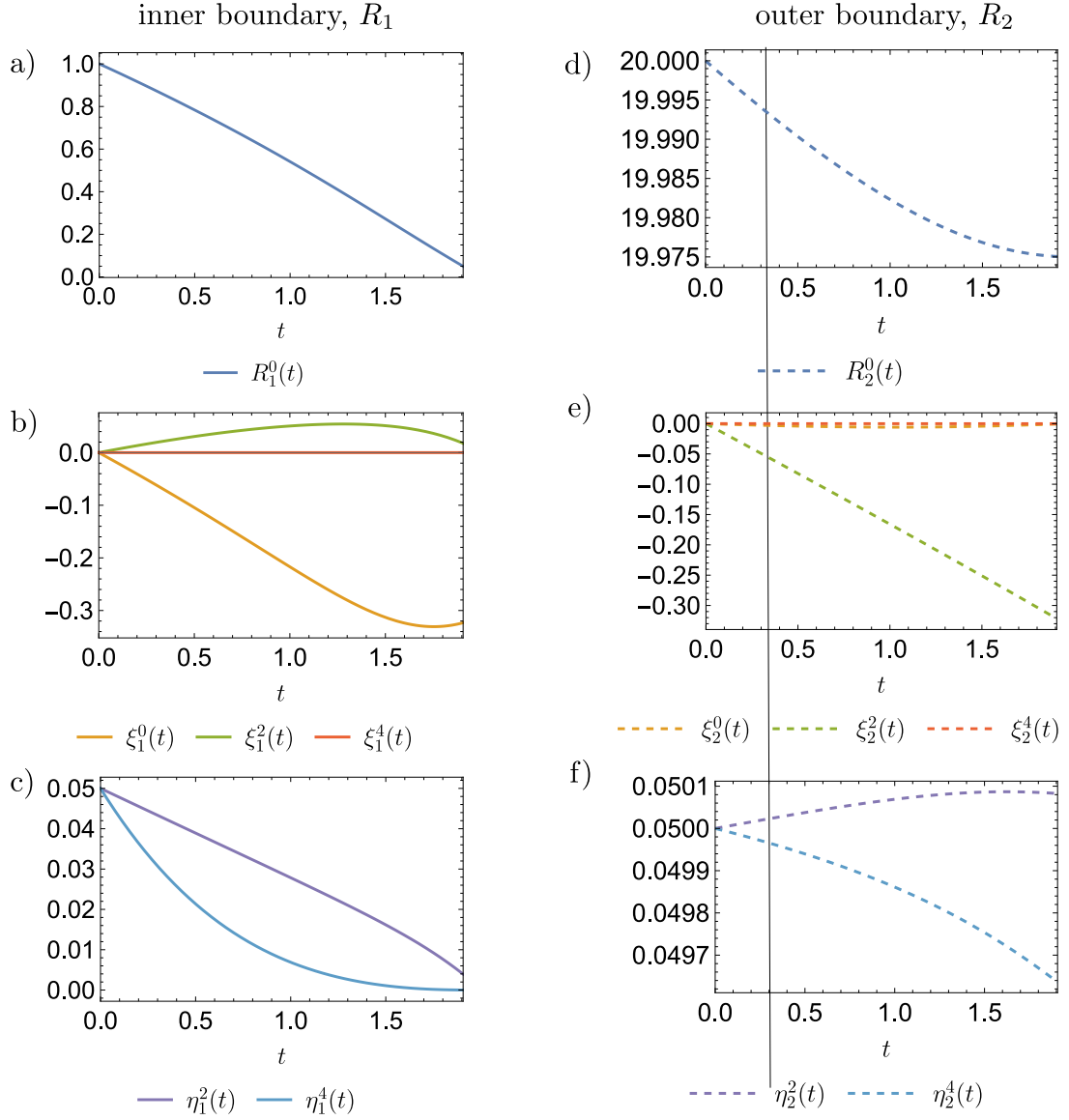


FIG. S1: Example of shape mode dynamics for the inner boundary, R_1 (a-c) and outer boundary R_2 (d-f). Plotted using $\Lambda = 0.1$ with initial conditions $R_1^0(0) = 1, R_2^0(0) = 20, \xi_i^k(0) = 0 \forall i, k$ and $\eta_i^k(0) = 0.05 \forall i, k$.

on R_1^0, R_2^0, Λ , (see code for explicit expressions) however ultimately reduce to expressions of the form:

$$\begin{aligned}
 \dot{\xi}_1^0 &= -\Delta_1^0 - a_1^0 \xi_1^0, \\
 \dot{\xi}_1^2 &= \Delta_1^2 - a_1^2 \xi_1^2 + b_1^2 \xi_2^2, \\
 \dot{\xi}_1^4 &= \Delta_1^4 - a_1^4 \xi_1^4 - b_1^4 \xi_2^4 \\
 \dot{\eta}_1^2 &= -c_1^2 \eta_1^2 + d_1^2 \eta_2^2, \\
 \dot{\eta}_1^4 &= -c_1^4 \eta_1^4 - d_1^4 \eta_2^4,
 \end{aligned} \tag{S36a}$$

for the inner boundary and

$$\begin{aligned}
\dot{\xi}_2^0 &= -\Delta_2^0 - a_2^0 \xi_1^0 + b_2^0 \xi_2^0, \\
\dot{\xi}_2^2 &= -\Delta_2^2 + a_2^2 \xi_1^2 - b_2^2 \xi_2^2, \\
\dot{\xi}_2^4 &= \Delta_2^4 + a_2^4 \xi_1^4 + b_2^4 \xi_2^4 \\
\dot{\eta}_2^2 &= c_2^2 \eta_1^2 - d_2^2 \eta_2^2, \\
\dot{\eta}_2^4 &= c_2^4 \eta_1^4 + d_2^4 \eta_2^4,
\end{aligned} \tag{S36b}$$

for the outer. Terms $\Delta_-^-, a_-^-, b_-^-, c_-^-, d_-^- > 0$ are all complicated functions of R_1^0, R_2^0, Λ . All modes have relaxational terms arising due to surface tension, however the $\xi_i^{0,2,4}$ modes are driven, as a consequence of activity in the bulk. These ODEs are integrated numerically to determine the shapes of the free boundaries as a function of time. Once the free boundary shape is known, the velocity, pressure and nematic texture fields are also determined, and the problem is solved. Figure S1 shows the typical time evolution of the shape mode amplitudes as a function of time during closure. We use $\beta_1 = \beta_2 = P = 1$ and stop integrating once R_1^0 drops below 5% of its initial value.

SUPPLEMENTARY RESULTS

Sensitivity of Inner Boundary to Presence of Outer Boundary

To investigate the effect of the outer boundary on our conclusions, we integrated ODEs (S36) for two values of $\Lambda = 0.1, 2$ and with different initial outer boundary radii, from $R_2^0(0) = 30$ down to $R_2^0(0) = 5$, fixing the inner boundary initial radius at $R_1^0(0) = 1$. We stopped integrating once $R_1^0 \leq 0.01$. Figure S2 shows the time evolution of shape modes for the inner boundary in each case.

For each value of Λ , the inner hole closed faster as the initial outer boundary radius decreased. Otherwise, there was little qualitative difference in the inner boundary shape dynamics as the outer radius was varied.

Value of Λ

Comparing the shape dynamics between values of Λ (Figure S3), we find that the shape mode amplitudes $\xi_1^{2,4}(t)$ generally attain greater maximum values for larger values of Λ (i.e. shorter nematic length scales $\sim 1/\Lambda$). That is, the wound boundary becomes more *anisotropic* as the nematic length scale decreases and the active bulk stress ($\nabla \cdot \mathbf{Q}^0$) is increasingly localised on the boundary. Examining the upper panels of Figure S2, we see that this result isn't special for this particular choice of the outer boundary initial radius. As discussed in the main text, this result suggests that the effective nematic length scale is relatively long because our experimental wounds were observed to remain approximately circular. The separate observation that correlations in alignment persist over many cell lengths confirms this prediction [S3].

Alternative nematic anchoring on inner boundary

To investigate the effect of our chosen boundary conditions on closure, we repeated the above calculation with normal anchored boundary conditions on the nematic texture at the inner wound boundary. The calculation follows the same steps as outlined above, except with normal anchoring on the nematic texture at R_1^0 :

$$Q_{xx}|_{R_1^0} = \beta_1 \cos 2\theta, \tag{S37a}$$

$$Q_{xy}|_{R_1^0} = \beta_1 \sin 2\theta. \tag{S37b}$$

Figure S4 illustrates the nematic texture surrounding the wound free boundary for $\Lambda = 0.1$ and the time evolution of the driven shape modes.

First, we note the positions of the two $-1/2$ defects now lie along the vertical $y = 0$ centreline. Second, the isotropic driven mode $\xi_1^0(t)$ is positive throughout closure. As such, contrary to the parallel anchored case, normal anchoring at the inner boundary requires *extensile* ($\alpha < 0$) active stresses to accelerate closure.

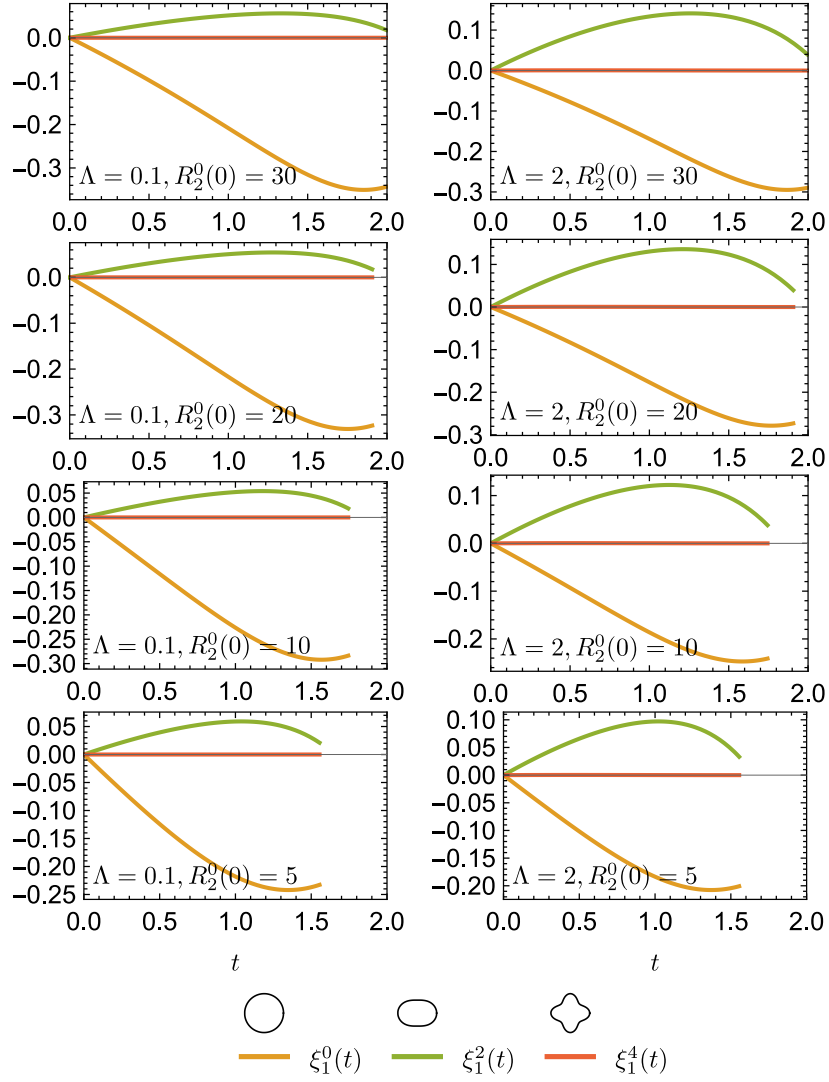


FIG. S2: Inner boundary shape mode dynamics for $\Lambda = 0.1$ (left) and $\Lambda = 2$ (right) for decreasing initial outer boundary radius $R_2^0(0)$. We observe little qualitative difference in the shape dynamics of the inner boundary as the outer boundary radius increases.

* h.andralojc@bristol.ac.uk

† rachel.bennett@bristol.ac.uk

‡ t.liverpool@bristol.ac.uk

- [S1] J. Turley, I. V. Chenchiah, P. Martin, T. B. Liverpool, and H. Weavers, Deep learning for rapid analysis of cell divisions in vivo during epithelial morphogenesis and repair, *eLife* **12**, RP87949 (2024).
- [S2] N. N. Lebedev and R. A. Silverman, *Special functions and their applications*, revised english edition ed., Selected Russian publications in the mathematical sciences (Prentice-Hall, Englewood Cliffs, N.J., 1965).
- [S3] J. Turley, *Deep learning and mathematical analysis of wound healing in flies; Live imaging in Drosophila*, Ph.D. thesis, University of Bristol (2023).

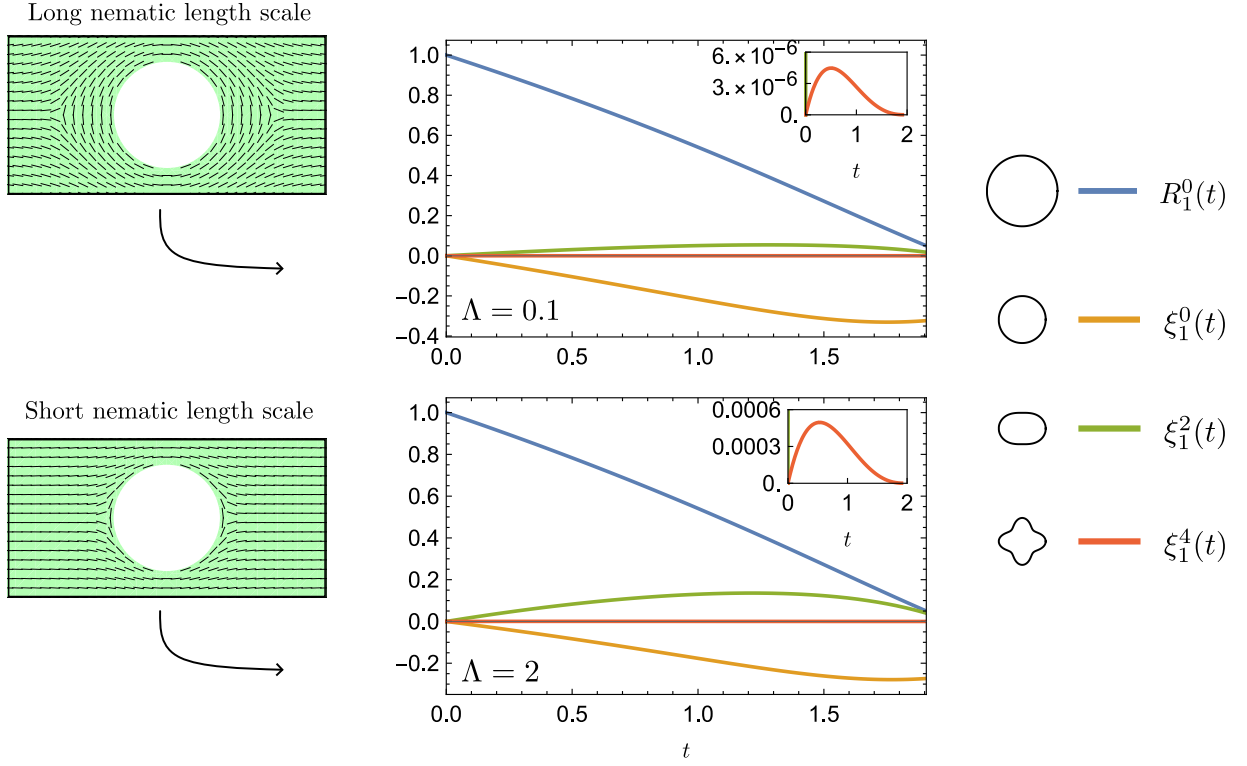


FIG. S3: Comparison of inner boundary shape evolution $R_1(\theta, t) = R_1^0 + \epsilon_\alpha (\xi_1^0 + \xi_1^2 \cos 2\theta + \xi_1^4 \cos 4\theta)$ for two values of $\Lambda = L/\ell_Q$. We find greater anisotropy in the shape of the inner boundary (greater shape mode amplitudes) as the nematic length scale is decreased.

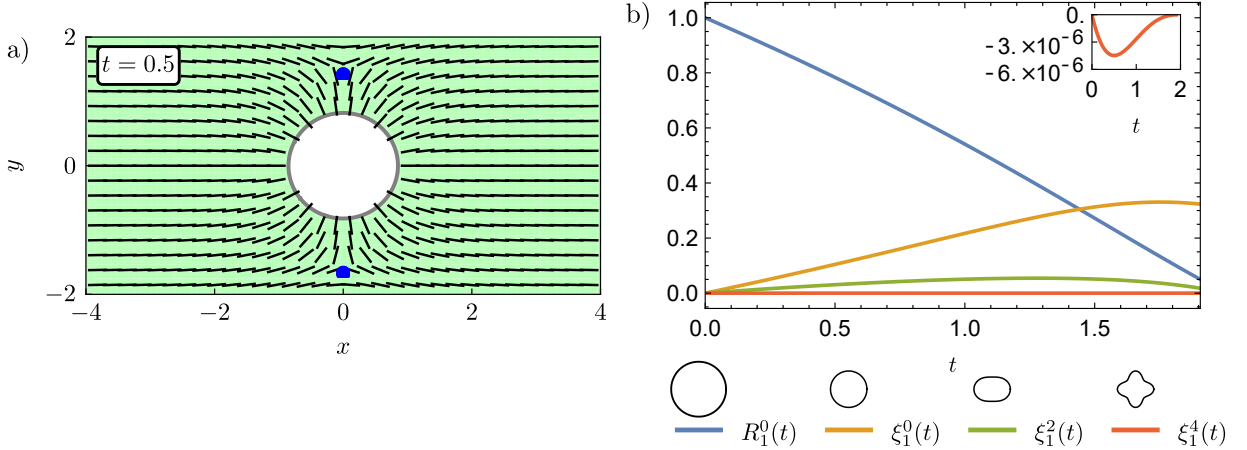


FIG. S4: (a) Illustration of the nematic texture surrounding the wound boundary with normal anchored boundary conditions on \mathbf{Q}^0 . (b) Inner boundary shape mode dynamics. Contrary to the parallel anchored case, contractile ($\alpha > 0$) active stresses decelerate closure. Plotted using $\Lambda = 0.1$.